Title

Deglacial reconstruction of the spatial extent and intensity of the North Atlantic Subtropical High

Authors

David Fastovich*[1] (ORCID: 0000-0002-0340-9819)
Tripti Bhattacharya[2] (ORCID: 0000-0002-5528-3760)
Stephen T. Jackson[3] (ORCID: 0000-0002-1487-4652)
Teresa R. Krause[4] (ORCID: 0000-0003-0211-5189)
James M. Russell[5] (ORCID: ?)
Timothy M. Shanahan[6] (ORCID: 0000-0002-3831-3198)
Chijun Sun[7] (ORCID: 0000-0002-3668-346X)
John W. Williams[8] (ORCID: 0000-0001-6046-9634)

*Corresponding author, fastovich@uga.edu
[1]Department of Geography, University of Georgia, Athens, GA, USA
[2]Department of Earth and Environmental Sciences, Syracuse University, Syracuse, NY, USA
[3]National and Regional Climate Adaptation Science Centers, U.S. Geological Survey, Tucson, AZ, USA, and Department of Geosciences, University of Arizona, Tucson, AZ, USA
[4]Department of Biology, Augsburg University, Minneapolis, MN, USA
[5]Department of Earth, Environmental & Planetary Sciences, Brown University, Providence, RI, USA
[6]Department of Earth and Planetary Sciences, Jackson School of Geosciences, The University of Texas at Austin, Texas, USA
[7]Department of Earth and Planetary Sciences, University of California, Davis, Davis, CA USA
[8]Department of Geography and Center for Climatic Research, University of Wisconsin-Madison, Madison, WI, USA

Peer-review Statement

This manuscript has been submitted to *Geophysical Research Letters* and is not peer-reviewed. This preprint has been submitted to EarthArXiv. Subsequent versions of this manuscript may have slightly different content. If accepted, the final version of this manuscript will be available via the 'Peer-reviewed Publication DOI' link on the right-hand side of this webpage.

CRediT (Contributor Roles Taxonomy)

David Fastovich - Conceptualization, Formal analyses, Funding acquisition, Investigation, Methodology, Project administration, Software, Validation, Visualization, Writing - original draft
Tripti Bhattacharya - Conceptualization, Funding acquisition, Investigation, Methodology, Resources, Supervision, Writing – review & editing
Stephen T. Jackson - Writing – review & editing, Investigation
Teresa R. Krause - Writing – review & editing, Investigation
James M. Russell - Writing – review & editing, Investigation
Timothy M. Shanahan - Writing – review & editing, Investigation
Chijun Sun - Writing – review & editing, Investigation
John W. Williams - Writing – review & editing, Investigation

Keywords

Hydroclimate, Leaf wax, precipitation isotopes, paleoclimate, deglaciation, atmospheric circulation

Abstract

Rainfall-related hazards are growing in southeastern North America (SENA) but well-documented climate-model biases cast doubt on projected rainfall changes. Using leaf-wax biomarkers (δD_{wax}) at White Pond, SC and Hall's Cave, TX, we reconstruct North Atlantic Subtropical High (NASH) variations across the last deglaciation (21 to 10 ka) to assess model fidelity. During the Younger Dryas, when Atlantic Ocean heat transport weakened, the NASH expanded westward, increasing rainfall in SENA. In contrast, the NASH gradually contracted eastward and weakened as deglacial greenhouse-gas concentrations increased, likely decreasing rainfall in SENA. An isotope-enabled simulation captures the first NASH response but severely underestimates the second. Because the NASH delivers moisture that drives extreme rainfall in SENA, this underestimation suggests that models cannot yet produce confident projections of regional rainfall extremes, or that those extremes will exceed current projections. Rainfall hazards facing SENA may be larger or less certain than current models suggest.

Plain Language Summary

Climate models, the primary tools used to predict long-term changes in rainfall, struggle to reproduce observed rainfall changes in southeastern North America (SENA), suggesting that future rainfall predictions are uncertain in the region. To address this limitation, we examine rainfall variability using the ratio of the two stable isotopes of hydrogen in precipitation (δD_p) in modern and paleoclimate settings. Modern observations indicate that δD_p in SENA responds to changes in the North Atlantic Subtropical High (NASH), an atmospheric circulation cell that transports moisture into SENA. We apply this relationship across the end of the last ice age using

leaf wax molecules preserved in lake sediments, whose hydrogen isotopes (δD_{wax}) record past precipitation. The NASH and associated moisture transport was strong at the end of the last ice age and weakened gradually as global temperatures increased, likely decreasing rainfall in the Atlantic Coastal Plain. Meanwhile, change in Atlantic Ocean circulation abruptly strengthened and expanded the NASH westward, and likely increased rainfall in the southern Great Plains. Climate models reproduce this abrupt response but cannot yet simulate the gradual weakening we observe, which suggests that future changes in extreme rainfall may be larger or less certain than previously thought.

Key Points

- Precipitation isotopes track North Atlantic Subtropical High (NASH) variability in eastern North America
- The NASH gradually weakened across the last deglaciation and strengthened abruptly during the Younger Dryas
- Climate models miss the deglacial weakening of the NASH-Great Plains pressure gradient, implying underestimated or uncertain extreme rainfall projections

1. Introduction

Subtropical high pressure systems are a prominent feature of global atmospheric circulation and influence hydroclimate globally (Rodwell and Hoskins, 2001). Northward moisture transport along the western edge of the North Atlantic Subtropical High (NASH) is the largest moisture source in southeastern North America (SENA) (Benton and Estoque, 1954; Rasmusson, 1967) where intensifying rainfall (Easterling et al., 2017; Zhao et al., 2023) threatens life, property, and economic activity. The cumulative cost of rainfall damages from flooding was between $39 and $91 billion from 1988 to 2017 across the United States (Davenport et al., 2021), with the greatest rainfall increases expected in SENA (Easterling et al., 2017). Accurate climate predictions are necessary to address these challenges, but simulating SENA precipitation using coupled land-atmosphere-ocean models is difficult in the region. The NASH is coupled to regional and North Atlantic sea surface temperature (SST, Hasanean, 2004; Rodwell and Hoskins, 2001) and the configuration of the Northern Hemisphere Hadley Cell (Grotjahn, 1993; Qiu et al., 2023). Substantial internal variability (e.g., North Atlantic Oscillation and Atlantic Multidecadal Variability) within each coupled component renders isolation and identification of specific processes governing SENA hydroclimate difficult. Constraining hydroclimate responses to different forcing mechanisms is needed to disentangle these controls and improve hydroclimate projections, which in turn requires longer-term perspectives than instrumental records can provide. Disentangling these controls in SENA has implications for hydroclimate projections in other subtropical regions because subtropical highs are governed by similar ocean-atmosphere couplings globally (Rodwell and Hoskins, 2001).

The most recent deglaciation is well-suited to constrain SENA hydroclimate response to forced changes in greenhouse gases, ice sheet configuration, and ocean circulation. Following the Last Glacial Maximum, atmospheric carbon dioxide increased by ~80 ppm (Marcott et al., 2014) which caused ice sheet loss (Clark et al., 2012; Dalton et al., 2020) and subsequent ocean heat transport variability (McManus et al., 2004). These forcings evolved asynchronously, and included both gradual and abrupt transitions, enabling isolation of their individual effects on SENA hydroclimate. However, a lack of unambiguous hydroclimate proxies has meant that few constraints exist for deglacial hydroclimate evolution in SENA. Fossil-pollen reconstructions have been among the few empirical approaches to understanding deglacial rainfall changes in SENA (Fastovich et al., 2022; Salonen et al., 2025; Shuman et al., 2019), but both traditional (Chevalier et al., 2020) and machine-learning approaches (Salonen et al., 2019) are limited by precipitation's secondary role in determining temperate forest composition (Juggins, 2013).

Leaf wax biomarkers can constrain the patterns and drivers of SENA hydroclimate. These long-chain *n*-alkanes are readily preserved in sediments across SENA, and their hydrogen isotopic signatures are significantly correlated to those of precipitation (δD_p) (Sachse et al., 2012). This proxy fidelity allows the application of leaf-wax stable isotope reconstructions to identify changes in atmospheric circulation, moisture sources, and precipitation amount across diverse environments (Bhattacharya et al., 2017; Fastovich et al., 2024; Feakins, 2013; Tierney et al., 2008). We examine hydroclimate dynamics across the last deglaciation in SENA using the hydrogen-isotope composition of leaf-wax biomarkers from White Pond, South Carolina (34.168 °N, 80.777 °W) and Hall's Cave, Texas (30.136 °N, 99.535 °W) (Sun et al., 2021). These records are used together to reconstruct the spatial extent and intensity of the NASH across the last deglaciation. The processes controlling deglacial evolution of the NASH are constrained with a suite of isotope-enabled climate models that provide insights into future rainfall extremes in SENA.

2. Methods

2.1 Leaf wax analyses and δD_{wax} measurements

White Pond, SC was cored in April 2015 (Krause et al., 2019) and sediments were processed using standard organic geochemical approaches to extract, purify, quantify, and measure the isotopic composition of C_{27} and C_{31} leaf wax biomarkers (Supplemental Text S1). We focus all δD_{wax} analyses at White Pond on C_{31} *n*-alkanes because of closer agreement to observational δD_p estimates (Supplemental Text S2, Figure S1).

We use existing δD_{wax} measurements from Hall's Cave, TX which only reported δD_{wax} for C_{27} *n*-alkanes (Supplementary Data 1 in Sun et al., 2021). Though these two sites represent differing

depositional environments, $\delta^{13}C_{wax}$ at White Pond and Hall's Cave agree well with fossil-pollen vegetation reconstructions suggesting a common, and comparable local source of leaf waxes to both sites (Krause et al., 2019; Sun et al., 2021). C_{31} $\delta^{13}C_{wax}$ at White Pond never increases above -28‰ consistent with low grass pollen abundance (<10% from 21 to 10 ka, Figure S2) (Figure 5 in Krause et al., 2019). Similarly, abrupt increases in $\delta^{13}C_{wax}$ at Hall's Cave are matched by increases in grass pollen abundance (Sun et al., 2021). Moreover, long chain *n*-alkanes ($\geq C_{27}$) are predominantly synthesized by high order land plants (Bush and McInerney, 2013; Ficken et al., 2000) suggesting comparable leaf wax provenance across the sites. We assess the influence of using different *n*-alkane chain lengths at White Pond (C_{31}) and Hall's Cave (C_{27}) by replicating our analyses using C_{27} δD_{wax} measurements from White Pond and find high agreement with results based on C_{31} δD_{wax} suggesting our conclusions are insensitive to this analytical choice (Figure S3).

2.2 Climate simulations and contemporary climate data products

We examine the transient, deglacial isotope-enabled iTRACE experiments (He, 2021) to identify the dynamics of hydroclimate variability in SENA. We compare deglacial iCESM simulations with transient deglacial experiments from two climate models that do not simulate water isotopes: CCSM3 (TraCE-21ka, He, 2011; Liu et al., 2009) and MPI-ESM1-2-CR (Kapsch et al., 2022). These experiments share similar transient changes to greenhouse gas concentrations, orbital configuration, and ice sheet topography, but differ in meltwater forcing. TraCE-21ka and iTRACE impose a meltwater forcing designed to reproduce proxy records of the AMOC which can be as much as three times more than global mean sea level rise (Ivanovic et al., 2018). Meanwhile, MPI-ESM1-2-CR meltwater fluxes are consistent with the ice sheet reconstruction forcing. We focus our results in iTRACE, but find that our conclusions are consistent across models regardless of differences in meltwater forcing (Supplemental Text S3).

The transient, deglacial experiments are compared against the iCESM simulations from Water Isotope Model Intercomparison Project (iCESM v1.3, WisoMIP) (Bong et al., 2026) experiments and the isotope-enabled Last Millennium Ensemble (iCESM v1, iLME) (Bong et al., 2026; Otto-Bliesner et al., 2016; Stevenson et al., 2019) to examine the sensitivity of the zonal δD_p gradient in southeastern North America to the NASH. The WisoMIP simulations span 1979-2023 and are performed with the atmosphere component of iCESM1.3 (i.e. iCAM5) and nudged to ERA5 reanalysis (Hersbach et al., 2020) to correct model biases (Bong et al., 2026). iLME spans the last millennium (850 to 2006 CE) with transient solar intensity, volcanic emissions, greenhouse gases, aerosols, land use conditions, and orbital parameters as forcings (Otto-Bliesner et al., 2016; Stevenson et al., 2019)

Alongside climate model simulations, we examine ERA5 reanalysis from 1940 to 2024 to investigate SENA hydroclimate coupling to the NASH (Hersbach et al., 2020). Together, this

suite of simulations lets us assess whether mean-state biases or the response to forcings drive misrepresentation of the zonal δD_p gradient–NASH relationship.

2.3 Bermuda High Index

In iTRACE, TraCE-21ka, MPI-ESM1-2-CR, and ERA5, we examine variability in the NASH using a modified version of the Bermuda High Index (BHI) from Zhu and Liang (2013). We select this formulation of the BHI as it was developed to investigate the influence of the NASH on regional climates in the United States by directly quantifying the pressure gradient between the Great Plains and NASH (Zhu and Liang, 2013). To account for forced shifts in NASH position from deglacial boundary conditions in our climate model experiments relative to ERA5, we shift the Gulf of Mexico region ten degrees east (Figure 1). In addition, we standardize mean sea level pressure before taking the difference between the Gulf of Mexico and Great Plains to allow both locations to equally contribute to the BHI. We examine the sensitivity of this analytical choice by comparing results using other NASH indices (Supplemental Text S3).

3. Results and Discussion

3.1 North Atlantic Subtropical High Influence on Contemporary δD_p

Contemporary climatology indicates a close link between hydrogen isotopes in precipitation (δD_p) and upstream variability in the NASH (Figure 1). Moisture from the Gulf of Mexico is the largest source of water vapor into SENA (Rasmusson, 1967) (Figure 1A). Zonal pressure gradients between SENA and the NASH are responsible for northward flow that delivers this moisture into SENA (Figure S4). Therefore, these northward winds and corresponding moisture advection into SENA are directly tied to the NASH.

Water vapor over the Gulf of Mexico is enriched in deuterium (Figure S5), making this moisture transport traceable in precipitation isotopes (δD_p). When advected into SENA, this vapor produces rainfall with a distinctly high δD_p (Figure 1A). Meanwhile, low meridional moisture transport in the Great Lakes, New England, and Canada indicates deuterium-depleted δD_p (Figure 1A).

The relationship between δD_p and meridional moisture transport in SENA suggests that northward transport of moisture from the Gulf of Mexico by the NASH is a primary control on SENA δD_p, overwhelming processes like distillation from continentality. For example, along a meridional transect at 88.5°W between 30–37.5°N, δD_p decreases 7‰ across 830 km of inland transport (Figure 1B). This decrease is far less than observed in other midlatitude regions such as the western United States, where δD_p decreases by 40‰ to 80‰ over 80 to 500 km (Ingraham and Taylor, 1991; Welker, 2000) and in Europe, where δD_p decreases by 16‰ over 1,000 km

(Rozanski et al., 1993) (here, we convert reported $\delta^{18}O_p$ values to δD_p, assuming equilibrium Rayleigh distillation).

3.2 A Regional Approach and Index for Reconstructing the North Atlantic Subtropical High Intensity and Extent

Compositing BHI values reveals two distinct hydroclimate responses across SENA to variability in the intensity and spatial extent of the NASH (Figure 1C, D). Under a westward-expanded (BHI ≥ 90th percentile) or eastern-contracted (BHI ≤ 10th percentile) NASH, meridional moisture transport anomalies are small along the Atlantic Coastal Plain (i.e. lowlands of Georgia, South Carolina, North Carolina, Figure 1C, 1D). Therefore, we posit that northward moisture flux into the Atlantic Coastal Plain records the *intensity* of meridional moisture transport along the western edge of the NASH. An increase in meridional moisture transport along the Atlantic Coastal Plain would increase δD_p from enhanced transport of deuterium-enriched vapor from the Gulf of Mexico (Figure S5). Meanwhile, prior analyses of δD_p in the southern Great Plains attribute decreases in δD_p to increases in stratiform rainfall from mesoscale convective systems fueled by moisture transport from the Great Plains Low Level Jet (Sun et al., 2019). The Great Plains Low Level Jet is coupled to the NASH through a geostrophic response to the zonal pressure gradient across the Great Plains (Song et al., 2019, 2018; Sun et al., 2021; Zhou et al., 2021). In this way, a westward expansion in the NASH leads to a large increase in northward moisture transport in the southern Great Plains (Figure 1C, 1D) and corresponding increase in the likelihood of mesoscale convective activity and decrease in δD_p (Sun et al., 2019). Therefore, unlike the positive relationship between the NASH, meridional moisture transport, and δD_p along the Atlantic Coastal Plain, a negative relationship is expected in the southern Great Plains. This suggests that unlike the Atlantic Coastal Plain, δD_p in the southern Great Plains is sensitive to the *spatial extent* of the NASH.

Asymmetric moisture flux responses in SENA to variability in the spatial extent and intensity of the NASH indicate that observations from both the Atlantic Coastal Plain and the southern Great Plains are needed to completely characterize the NASH, as either region alone conflates NASH intensity and spatial extent. We resolve this by taking the difference in δD_{wax} from a site in the Atlantic Coastal Plain (White Pond) and southern Great Plains (Hall's Cave) (Sun et al., 2021) after standardizing both records (Figure 2), to define a leaf-wax-based reconstruction of NASH variability, $\Delta\delta D\ NASH_{leaf\ wax}$ (Supplemental Information). The resulting zonal δD_{wax} gradient reconstructs the intensity (White Pond) and spatial extent (Hall's Cave) of the NASH in a way that a single-site reconstruction cannot. We reproduce $\Delta\delta D\ NASH_{leaf\ wax}$ using ERA5 meteorological variables in place of δD_{wax}: meridional vapor transport and average rainfall rate. Both correlate significantly with mean sea level pressure over the Gulf of Mexico (reflecting NASH spatial extent) and over the western Atlantic (reflecting NASH intensity), supporting our use of zonal δD_{wax} gradients in SENA to reconstruct the spatial extent and intensity of the NASH

(Figure S6). We also use PRYSM (Dee et al., 2015) to develop pseudoproxy δD_{wax} records at White Pond and Hall's Cave from iTRACE δD_p and find that $\Delta\delta D$ $NASH_{leaf\ wax}$ can successfully reconstruct atmospheric reorganization in the North Atlantic across the last deglaciation (Supplemental Text S4).

3.3 Asymmetric North Atlantic Subtropical High response across the last deglaciation

At White Pond, δD_{wax} remains high until ~15 to 14 ka, indicating elevated transport of deuterium-enriched δD_{vapor} moisture from the Gulf of Mexico into the southeastern United States, driven by a stronger NASH. A subsequent gradual decrease in δD_{wax} at White Pond tracks ice sheet loss, suggesting a gradual decrease in northward moisture from a weakening of the NASH in response to increasing temperatures (Figure 2A). A gradual weakening of the NASH is supported by a gradual decrease in dune activity in southern Europe across the last deglaciation into the Holocene (Costas et al., 2016). In contrast, δD_{wax} at Hall's Cave, TX demonstrates high millennial-scale variability (Figure 2B). Deglacial millennial-scale variability in NASH wind speed has previously been shown to be inversely related to north Atlantic SSTs (Brauer et al., 2008). The similarity between Hall's Cave δD_{wax} and north Atlantic SSTs (Figure 2B) supports the interpretation that a westward expansion of the NASH from decreased SSTs would increase stratiform rainfall and decrease δD_{wax}.

Combining White Pond and Hall's Cave δD_{wax} into a reconstruction of the intensity and spatial extent of NASH ($\Delta\delta D$ $NASH_{leaf\ wax}$, Figure 2C) identifies two distinct modes of behavior. The first mode is a weakening and contraction of the NASH in response to deglacial warming between 15.4 and 10.5 ka (Figure 2C). The second mode is an abrupt intensification and expansion in response to a weakening of the Atlantic Meridional Overturning Circulation (AMOC) that operates at millennial timescales and is particularly evident between 13.7 ka and 12 ka (Figure 2C).

Gradual weakening and contraction of the NASH in the first mode is indicated by the decrease in $\Delta\delta D$ $NASH_{leaf\ wax}$ from ~1 at 15.4 ka to ~-2 at 10.5 ka. Positive $\Delta\delta D$ $NASH_{leaf\ wax}$ between 18 ka and 15 ka reflect above-average δD_{wax} at White Pond, driven by a stronger NASH that increases the flux of deuterium-enriched Gulf of Mexico water vapor into the site (Figure 2). During this same interval Hall's Cave δD_{wax} is below average from increased stratiform rainfall, fueled by elevated Gulf of Mexico moisture transport, thereby increasing the zonal δD_{wax} gradient across SENA (Figure 2). Collectively, these site-level changes, summarized in $\Delta\delta D$ $NASH_{leaf\ wax}$, suggest that the late-glacial (18 ka to 15 ka) NASH was stronger and larger relative to the Holocene (11 ka to 10 ka). The NASH weakened after ~15 ka as White Pond δD_{wax} decreased below mean values and contracted eastward as Hall's Cave δD_{wax} increased above mean values (Figure S7). High moisture flux between 18 ka and 15 ka suggests elevated late-glacial precipitation that declined into the Holocene.

Large Northern Hemisphere ice loss at ~14 ka may explain the long-term NASH weakening and contraction inferred from $\Delta\delta D\ NASH_{leaf\ wax}$ (Figure 2). Northern Hemisphere ice loss would have decreased albedo and reduced the Northern Hemisphere meridional temperature gradient, weakening Hadley Cell subsidence in the subtropics and the NASH. This proposed mechanism is consistent with Last Glacial Maximum climate model experiments, in which high albedo produces an intensified NASH (Pausata et al., 2011).

An abrupt increase in the $\Delta\delta D\ NASH_{leaf\ wax}$ ~1 from 13.7 ka to 12 ka and overlapping with the Younger Dryas (12.9 to 11.7 ka) suggests a westward expansion of the NASH may be associated with decreases in north Atlantic SSTs from a reduction in the AMOC (Figure 2). A westward expansion of the NASH beginning at 13.7 ka decreases δD_{wax} at Hall's Cave below mean values from increased stratiform rainfall fueled by concentrated moisture transport toward Hall's Cave from an expanded NASH, increasing $\Delta\delta D\ NASH_{leaf\ wax}$ (Figure 2C, S7). White Pond δD_{wax} shows no abrupt deviation, suggesting NASH intensity did not change appreciably during this interval, only its spatial extent (Figure 2C, S7). This NASH configuration would have driven enhanced northward moisture transport along an expanded western flank of the NASH and increased precipitation in the Great Plains consistent with increased hydroclimate-sensitive tree taxa abundance at Cupola Pond, MO between ~15 and ~11 ka (Jones et al., 2017).

Our reconstruction directly probes the intensity and spatial extent of NASH and clarifies that the NASH may not only have intensified from AMOC weakening, as previously inferred (Baldini et al., 2015; Brauer et al., 2008; Fastovich et al., 2020), but also expanded westward (Figure 2). Alternatively, the NASH may have expanded westward without intensification. An intensification and expansion, or a westward expansion alone, of the NASH is likely linked to changes in the Northern Hemisphere meridional temperature gradient, the same mechanism proposed for the greenhouse-gas-driven weakening of the NASH. The two responses differ in pace because deglacial AMOC perturbations were abrupt (Figure 2D), while ice sheet loss was gradual and monotonic (Figure 2A). During the Younger Dryas, a weakening of the AMOC abruptly cooled SSTs in the north Atlantic from reduced ocean heat transport (Figure 2B) which would have increased the Northern Hemisphere meridional temperature gradient, Hadley circulation subsidence (McGee et al., 2018), and the NASH. In addition, lower SSTs may have directly increased NASH intensity and spatial extent by increasing air density and mean sea level pressure.

However, Heinrich Event 1 likely had a larger reduction in the AMOC (McManus et al., 2004), yet $\Delta\delta D\ NASH_{leaf\ wax}$ suggests little change to the NASH (Figure 2C, 2D). We propose that the sensitivity of NASH extent to AMOC perturbations depends on background climate state. Under nearly full-glacial boundary conditions (as during Heinrich Event 1), the NASH response is muted, whereas under intermediate conditions (as during the Younger Dryas), the NASH

response is pronounced. This may be because sea ice extent was already extensive before Heinrich event cooling initiated (El bani Altuna et al., 2024). A second, potentially complementary, explanation involves ice-sheet configuration: the Laurentide Ice Sheet changed little until ~14 ka, when the Cordilleran and Laurentide ice sheets separated (Gregoire et al., 2012). This separation would have warmed the land surface (Sun et al., 2021), steepening the zonal temperature gradient and strengthening the NASH (Song et al., 2018), which could explain why the $\Delta\delta D\ NASH_{leaf\ wax}$ increase at 13.7 ka leads Younger Dryas AMOC weakening by ~800 years (Figure 2).

3.4 Simulations of the North Atlantic Subtropical High and Proxy-Model Comparisons

In all isotope-enabled climate simulations, we reproduce $\Delta\delta D\ NASH_{leaf\ wax}$ with simulated δD_p by taking the standardized difference between simulated δD_p for the four grid cells surrounding White Pond and Hall's Cave, to define $\Delta\delta D\ NASH_{iCESM}$. We distinguish the proxy reconstruction ($\Delta\delta D\ NASH_{leaf\ wax}$) from its model analogue ($\Delta\delta D\ NASH_{iCESM}$) using subscripts. For each iCESM experiment we take the difference between high (≥ 90th percentile) and low $\Delta\delta D\ NASH_{iCESM}$ years (≤ 10th percentile), which demonstrate that the zonal δD_p gradient across SENA appears closely coupled with the NASH (Figure 3).

In a simulation from 1979-2023 nudged to ERA5 reanalysis (WisoMIP) (Bong et al., 2026) and an un-nudged simulation of the last millennium (iLME, 850 to 2006) (Otto-Bliesner et al., 2016; Stevenson et al., 2019), the zonal δD_p gradient increases as expected when the NASH expands westward, in agreement with our contemporary δD_p analyses and δD_{wax} proxy inferences (Figure 3A, 3B). However, in a transient, deglacial simulation (iTRACE) with greenhouse gas, ice sheet extent, ocean heat transport, and orbital forcings derived from proxy observations (He, 2021), the simulated zonal δD_p gradient across SENA increases when the NASH weakens and contracts eastward: an opposite relationship to our proxy records (Figure 3D). These findings indicate that iCESM1 accurately simulates the relationship between the zonal δD_p gradient in SENA and the NASH, but that the model struggles when forcings beyond those of the last millennium or historical period are introduced. This modeling challenge is caused, in part, by the response of the Intertropical Convergence Zone to the AMOC which is erroneously linked to meridional moisture flux and corresponding δD_p at Hall's Cave in iTRACE (Supplemental Text S4).

Despite these modeling challenges, iTRACE, TraCE-21ka, and MPI-ESM1-2-CR partly simulates the response of the NASH to a weakening of the AMOC. Applying the same BHI defined from reanalysis (Section 2.2) to simulated pressure fields in all models, enables comparing the simulated NASH to $\Delta\delta D\ NASH_{leaf\ wax}$. The simulated NASH matches the millennial-scale variability in $\Delta\delta D\ NASH_{leaf\ wax}$ (Figure 4), which propagates to simulated integrated vapor transport (Figure S8-S10) and δD_p in iTRACE (Figure 4). High BHI values during periods of meltwater addition (18-14 ka for iTRACE and TraCE-21ka; 14.7-13.6 ka and

13-12.2 ka for MPI-ESM1-2-CR) demonstrates that the NASH intensified and expanded westward, which increased simulated moisture flux at White Pond (Figure 4, S8-S10). These coupled changes between simulated meridional vapor transport at White Pond and BHI appear linked to simulated SSTs in the North Atlantic (Figure 4E), and therefore the AMOC. Low North Atlantic SSTs force an intensification and expansion of the NASH, indicated by high BHI values, with downstream increases in meridional vapor transport at White Pond (Figure 4, S8-S10). Critically, however, all climate models fail to simulate a weakening in the pressure gradient between the NASH and Great Plains because unstandardized BHI values for the Holocene (12 ka to 11 ka) are higher than the late-glacial (20 ka to 19 ka) (Figure S8B, S9B, S10B).

This failure carries a troubling implication when extended to future extreme rainfall projections. Extreme rainfall is likely to become more common in SENA (Easterling et al., 2017), with increases in SENA fall rainfall already linked to variability in the NASH (Bishop et al., 2019). Yet, iTRACE, TraCE-21ka, and MPI-ESM1-2-CR reveal that models dramatically underestimate the NASH-Great Plains pressure gradient response to greenhouse gas increases, and therefore the moisture flux that supplies rainfall (Figure S7C, S7D, S7E, S8-S10). Since extreme rainfall scales with mean rainfall rates (Pendergrass and Hartmann, 2014) and meridional moisture flux is a key ingredient for extreme rainfall in SENA (Teale and Robinson, 2022), these models are likely also underestimating past extreme rainfall. When placed alongside current extreme rainfall projections, our results support two conclusions. In the best case, ESMs may not produce confident projections of regional extreme rainfall. In the worst case, extreme rainfall in SENA may exceed the latest Earth System Model projections because these very models underestimate the pressure gradient response in the past.

4. Conclusions

Our results demonstrate that the zonal δD_p and δD_{wax} gradient across SENA records changes in moisture delivered by the NASH. Using this regional gradient, we show that the NASH weakened and contracted in response to gradual warming across the last deglaciation, which likely drove gradual drying in SENA. However, the NASH intensified in response to a weakening in Atlantic Ocean heat transport, likely increasing precipitation in SENA. A transient, isotope-enabled climate model experiment accurately simulates the responses of the NASH to a weakening of ocean heat transport, but underestimates responses to gradual deglacial warming. Because Northern Hemisphere subtropical highs are expected to strengthen into the future (Li et al., 2012), leading to increases in projected rainfall extremes in SENA (Easterling et al., 2017), the inability of three transient deglacial climate simulations to accurately simulate the response of the NASH-Great Plains pressure gradient to greenhouse-gas induced warming suggests that past and future simulations of extreme rainfall are poorly constrained and possibly underestimated. Future rainfall hazards may be less certain, and substantially larger, than currently projected.

Acknowledgements

We gratefully acknowledge technical support from the Georgia Advanced Computing Resource Center and Stephanie Bullinger (Syracuse University). DF and TB acknowledge funding support from the National Science Foundation award AGS-2402498. TB acknowledges support from NSF CAREER Grant OCE-2237502 and Sloan Foundation Fellowship FG-2023-20259. White Pond was cored with support from NSF DEB-1353896. Initial lipid extraction at White Pond was supported by NSF DEB-1349662 and leaf wax biomarker measurements were made possible with support from NSF MRI Grant EAR-2018078. We thank two anonymous reviewers for their helpful feedback on the manuscript. Claude Opus was used for code debugging and grammar checking.

Source Data

All data, including derived climate model fields (integrated vapor transport), along with analysis code and a containerized computing environment, are available on Zenodo (Fastovich et al., 2026). The original climate model output is not included due to its size but freely available from the National Science Foundation National Center for Atmospheric Research Geoscience Data Exchange (Otto-Bliesner et al., 2021, 2025), the NASA Center for Climate Simulation (Bong et al., 2026), and the World Data Center for Climate (dataset acronym PMMXMCR). White Pond, SC δD_{wax} and $\delta^{13}C_{wax}$ measurements are also freely accessible on the NOAA Paleoclimatology Database and Zenodo (Fastovich et al., 2026). Hall's Cave, TX δD_{wax} is also accessible in the supplemental information of the original publication (Sun et al., 2021).

Conflict of Interest

The authors declare no conflicts of interest relevant to this study.

Figures

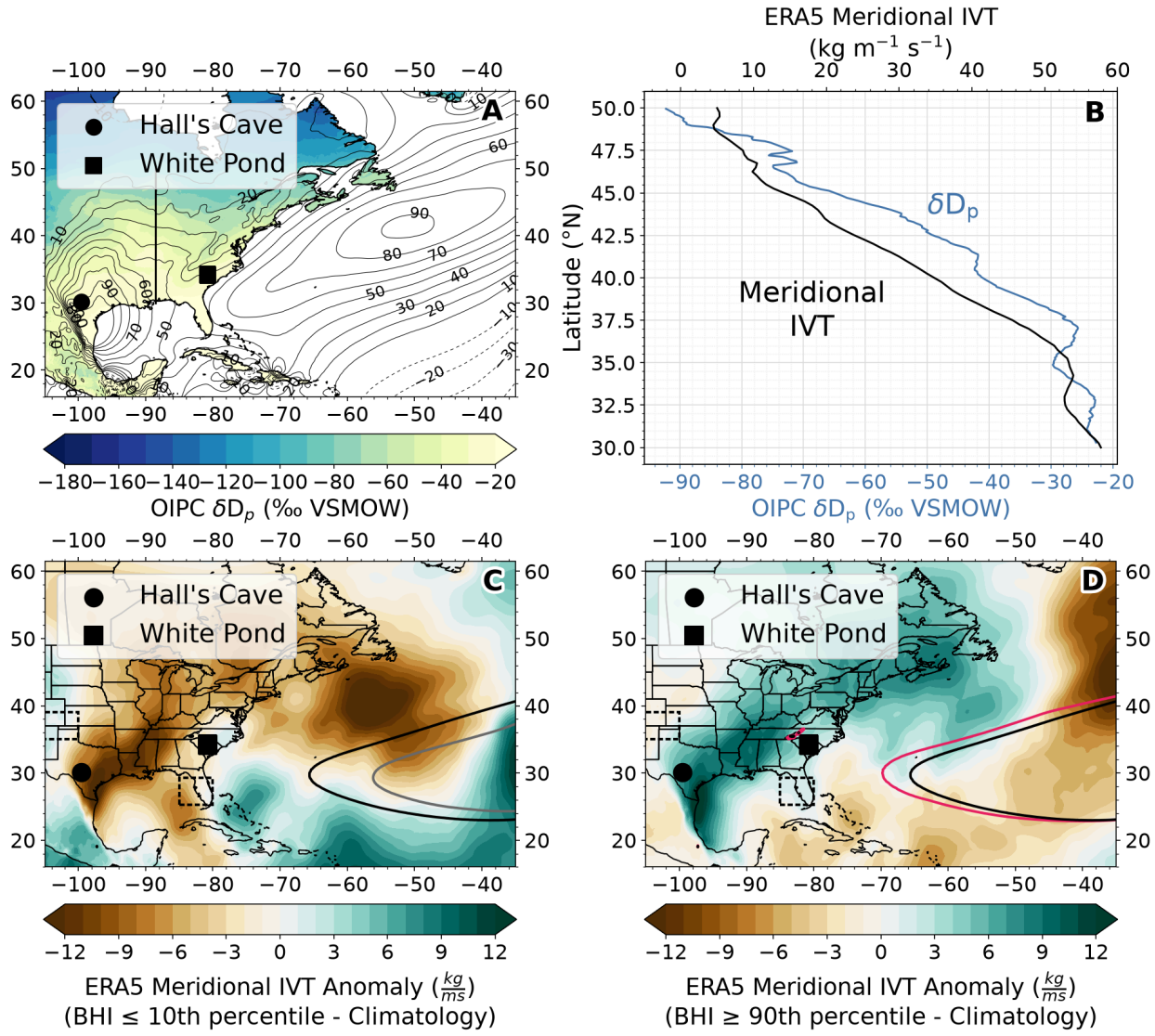


Figure 1. The relationship between meridional moisture transport, δD_p, and the North Atlantic Subtropical High in southeastern North America, and the contrasting signals recorded by Hall's Cave and White Pond during shifts in North Atlantic Subtropical High spatial extent. (A) The contemporary climatology of δD_p in SENA, where the filled contours correspond to δD_p and the black contours correspond to meridional integrated vapor transport from ERA5 with the 0 contour omitted. The black vertical line shows the transect presented in B. (B) A latitudinal transect at 88.5°W of integrated vapor transport (black line) and δD_p (blue line) between 30°and 50°N. δD_p values are from the Online Isotopes in Precipitation Calculator (Bowen, 2025). (C) Map of meridional integrated vapor transport anomalies (filled contours) for an eastward contraction (BHI ≤ 10th percentile) of the NASH relative to the 1940 to 2024 average. The black contour corresponds to the climatological position of the 1019 hPa isobar, while the gray contour corresponds to the 1019 hPa isobar under an eastward contraction of the NASH. D) As in C but for a westward expansion with the pink contour corresponding to the

1019 hPa isobar under a westward expansion of the NASH (BHI ≥ 90th percentile) of the NASH. Black dashed boxes in (C) and (D) correspond to the regions used to calculate BHI. In all mapped panels, the circle indicates Hall's Cave and the square indicates White Pond; these sites record contrasting signals during shifts in NASH intensity and spatial extent.

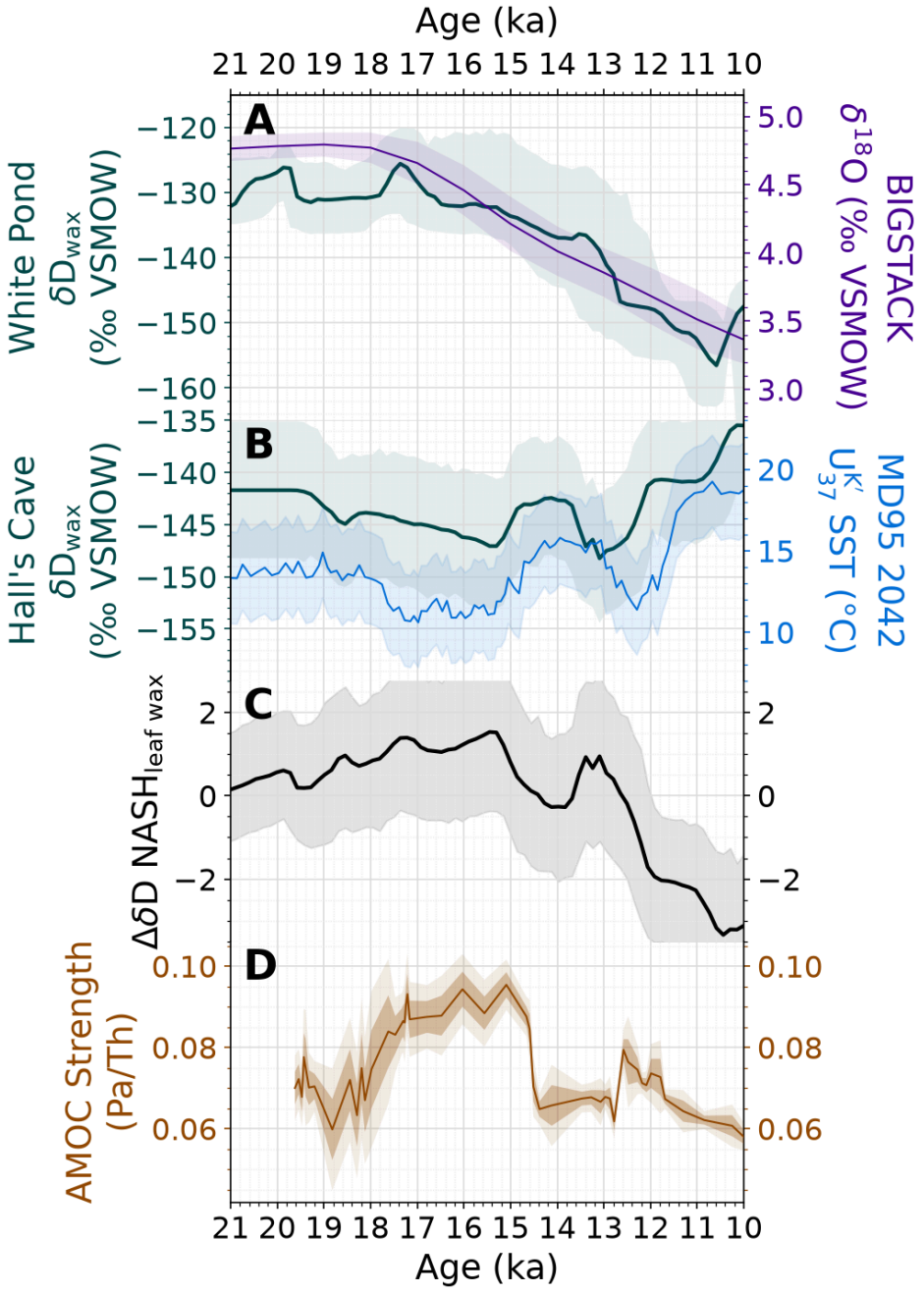


Figure 2. North Atlantic Subtropical High evolution during the last deglaciation. (A) Median White Pond δD_{wax} (green line, green shading represents the 95% CI) from a resampling approach that propagates measurement and temporal uncertainty compared to benthic foraminifera $\delta^{18}O$, a proxy for global ice volume (purple line, purple shading represents 1-σ measurement and temporal uncertainty) (Zhou et al., 2026). (B) As in (A), but for Hall's Cave δD_{wax}, plus reconstructed north Atlantic SSTs from MD95 2042 (Davtian and Bard, 2023) (shading representing the 95% CI). (C) Median Δδ D NASH$_{leaf\ wax}$ values calculated as the standardized difference in δD_{wax} between White Pond and Hall's Cave (black line, gray shading represents the 95% CI), with temporal and measurement uncertainty propagated. (D) Reconstructed AMOC variability based on Pa/Th ratios in sediment cores from Bermuda Rise (McManus et al., 2004), with larger values representing a weaker AMOC (dark and light shading represent the 1-σ and 2-σ measurement uncertainty, respectively). A map of all site is present in the Supplemental Information (Figure S11).

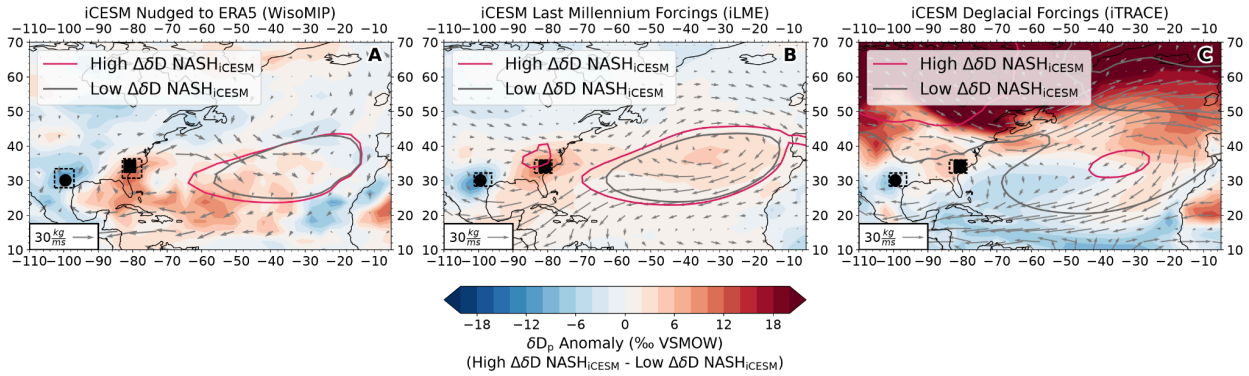


Figure 3. Isotopic fingerprint of the North Atlantic Subtropical High. Composites of mean sea level pressure (contours), integrated vapor transport (vectors), and δD_p (filled contours) from three iCESM experiments for high (≥ 90th percentile) - low (≤ 10th percentile) ΔδD $NASH_{iCESM}$ years (Bong et al., 2026; He, 2021; Otto-Bliesner et al., 2016; Stevenson et al., 2019). ΔδD $NASH_{iCESM}$ is defined identically to ΔδD $NASH_{leaf\ wax}$: the standardized difference between the four grid cells bounding White Pond and Hall's Cave simulated δD_p (dashed boxes around each site). For each experiment, the integrated vapor transport vectors and δD_p filled contours show the anomaly between high-ΔδD $NASH_{iCESM}$ and low-ΔδD $NASH_{iCESM}$ years. In contrast, the pink contour shows mean sea level pressure during high-ΔδD $NASH_{iCESM}$ years, while the gray contour shows mean sea level pressure during low-ΔδD $NASH_{iCESM}$ years, so the two contours together reveal how the simulated NASH shifts in spatial extent and intensity. Note, given the different underlying boundary conditions we present the 1020 hPa contour in (A) and (B), but the 1030 hPa contour in (C).

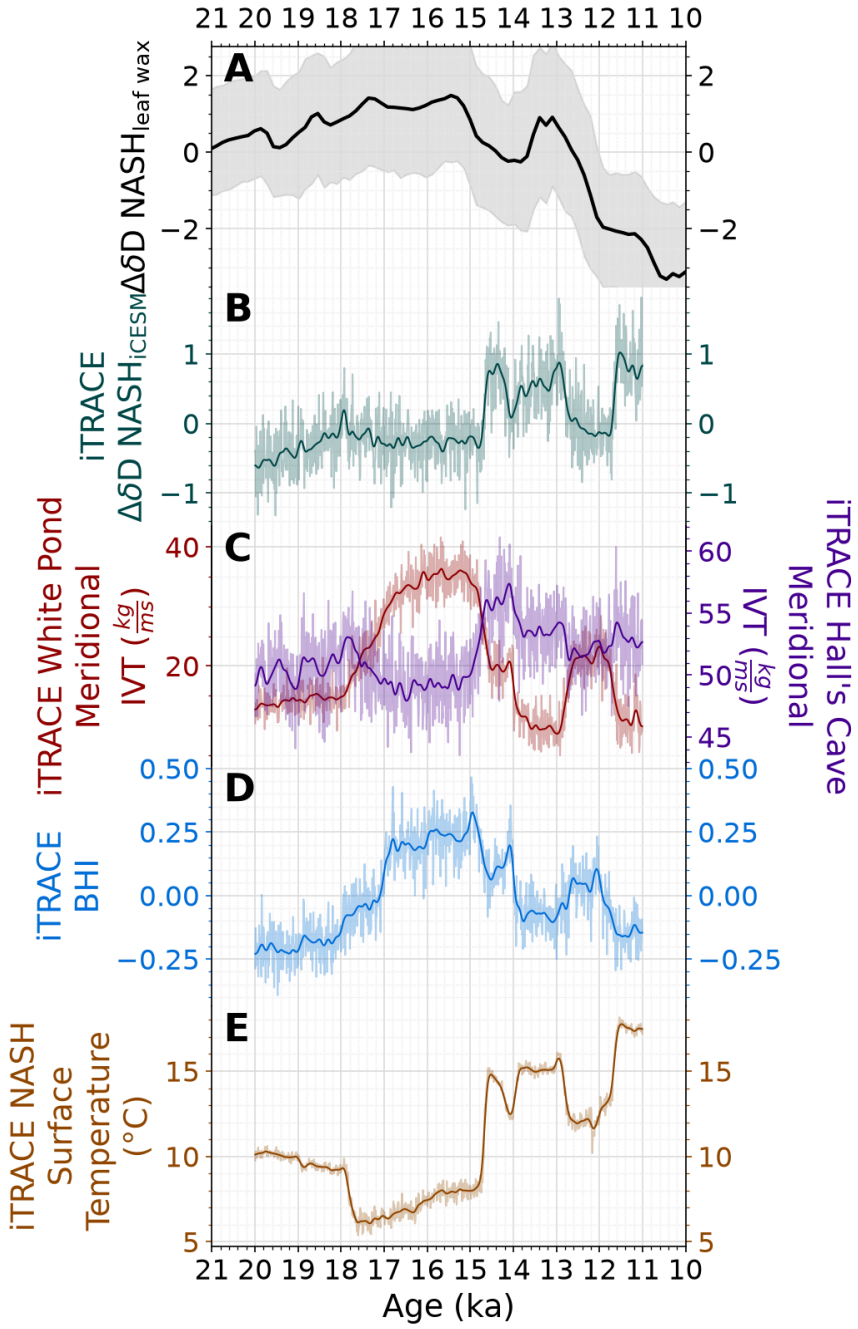


Figure 4. iTRACE deglacial hydroclimate dynamics. (A) Median $\Delta\delta D\ NASH_{leaf\ wax}$ values calculated as the standardized difference in δD_{wax} between White Pond and Hall's Cave (black line, gray shading represents the 95% CI), with temporal and measurement uncertainty propagated. (B) $\Delta\delta D\ NASH_{iCESM}$ calculated identically to (A) but from simulated δD_p for the four grid cells bounding White Pond and Hall's Cave from iTRACE. (C) Simulated meridional integrated vapor transport at White Pond (red line) and Hall's Cave (purple line). (D) Simulated iTRACE BHI, as used in Figure 1C and 1D. (E) Simulated North Atlantic iTRACE SST, averaged between 35° to 40°N and 55° to 65°W. In panels B to E the light lines correspond to decadal averages and the dark lines correspond to a Gaussian low-pass filter (σ = 50 years).

References

Baldini, L.M., McDermott, F., Baldini, J.U.L., Arias, P., Cueto, M., Fairchild, I.J., Hoffmann, D.L., Mattey, D.P., Muller, W., Nita, D.C., Ontanon, R., Garcia-Monco, C., Richards, D.A., 2015. Regional temperature, atmospheric circulation, and sea-ice variability within the Younger Dryas Event constrained using a speleothem from northern Iberia. Earth Planet. Sci. Lett. 419, 101–110. https://doi.org/10.1016/j.epsl.2015.03.015

Benton, G.S., Estoque, M.A., 1954. Water-vapor transfer over the North American continent. J. Atmos. Sci. 11, 462–477. https://doi.org/10.1175/1520-0469(1954)011%3C0462:WVTOTN%3E2.0.CO;2

Bhattacharya, T., Tierney, J.E., DiNezio, P., 2017. Glacial reduction of the North American Monsoon via surface cooling and atmospheric ventilation. Geophys. Res. Lett. 44, 5113–5122. https://doi.org/10.1002/2017gl073632

Bishop, D.A., Williams, A.P., Seager, R., 2019. Increased fall precipitation in the southeastern United States driven by higher-intensity, frontal precipitation. Geophys. Res. Lett. 46, 8300–8309. https://doi.org/10.1029/2019gl083177

Blaauw, M., Christen, J.A., 2011. Flexible paleoclimate age-depth models using an autoregressive gamma process. Bayesian Anal. 6, 457–474.

Bong, H., LeGrande, A.N., Dee, S., Zhu, J., Cauquoin, A., Fiorella, R.P., Ding, Q., Dutrievoz, N., Tanoue, M., Frazer, M., Sarkar, M., Agosta, C., Yoshimura, K., Werner, M., Okazaki, A., Risi, C., Steen-Larsen, H.C., Casado, M., Wahl, S., Nusbaumer, J., Worden, J., Good, S., Bailey, A., Schneider, M., Noël, S., Mandal, S., Bowman, K., Li, Y., Schmidt, G.A., 2026. Water Isotope Model Intercomparison Project (WisoMIP): Present-Day Climate. J. Geophys. Res. Atmos. 131, e2025JD044985. https://doi.org/10.1029/2025JD044985

Bowen, G.J., 2025. Gridded maps of the isotopic composition of meteoric waters.

Brauer, A., Haug, G.H., Dulski, P., Sigman, D.M., Negendank, J.F.W., 2008. An abrupt wind shift in western Europe at the onset of the Younger Dryas cold period. Nat. Geosci. 1, 520–523. https://doi.org/10.1038/ngeo263

Bush, R.T., McInerney, F.A., 2013. Leaf wax *n*-alkane distributions in and across modern plants: Implications for paleoecology and chemotaxonomy. Geochim. Cosmochim. Acta 117, 161–179. https://doi.org/10.1016/j.gca.2013.04.016

Chevalier, M., Davis, B.A.S., Heiri, O., Seppa, H., Chase, B.M., Gajewski, K., Lacourse, T., Telford, R.J., Finsinger, W., Guiot, J., Kuhl, N., Maezumi, S.Y., Tipton, J.R., Carter, V.A., Brussel, T., Phelps, L.N., Dawson, A., Zanon, M., Valle, F., Nolan, C., Mauri, A., de Vernal, A., Izumi, K., Holmstrom, L., Marsicek, J., Goring, S., Sommer, P.S., Chaput, M., Kupriyanov, D., 2020. Pollen-based climate reconstruction techniques for late Quaternary studies. Earth-Sci. Rev. 210, 33. https://doi.org/10.1016/j.earscirev.2020.103384

Clark, P.U., Shakun, J.D., Baker, P.A., Bartlein, P.J., Brewer, S., Brook, E.J., Carlson, A.E., Cheng, H., Kaufman, D.S., Liu, Z., Marchitto, T.M., Mix, A.C., Morrill, C., Otto-Bliesner, B.L., Pahnke, K., Russell, J.M., Whitlock, C., Adkins, J.F., Blois, J.L., Clark, J., Colman, S.M., Curry, W.B., Flower, B.P., He, F., Johnson, T.C., Lynch-Stieglitz, J., Markgraf, V., McManus, J.F., Mitrovica, J.X., Moreno, P.I., Williams, J.W., 2012. Global climate evolution during the last deglaciation. Proc. Natl. Acad. Sci. https://doi.org/10.1073/pnas.1116619109

Costas, S., Naughton, F., Goble, R., Renssen, H., 2016. Windiness spells in SW Europe since the last glacial maximum. Earth Planet. Sci. Lett. 436, 82–92. https://doi.org/10.1016/j.epsl.2015.12.023

Dalton, A.S., Margold, M., Stokes, C.R., Tarasov, L., Dyke, A.S., Adams, R.S., Allard, S., Arends, H.E., Atkinson, N., Attig, J.W., Barnett, P.J., Barnett, R.L., Batterson, M., Bernatchez, P., Borns, H.W., Breckenridge, A., Briner, J.P., Brouard, E., Campbell, J.E., Carlson, A.E., Clague, J.J., Curry, B.B., Daigneault, R.-A., Dubé-Loubert, H., Easterbrook, D.J., Franzi, D.A., Friedrich, H.G., Funder, S., Gauthier, M.S., Gowan, A.S., Harris, K.L., Hétu, B., Hooyer, T.S., Jennings, C.E., Johnson, M.D., Kehew, A.E., Kelley, S.E., Kerr, D., King, E.L., Kjeldsen, K.K., Knaeble, A.R., Lajeunesse, P., Lakeman, T.R., Lamothe, M., Larson, P., Lavoie, M., Loope, H.M., Lowell, T.V., Lusardi, B.A., Manz, L., McMartin, I., Nixon, F.C., Occhietti, S., Parkhill, M.A., Piper, D.J.W., Pronk, A.G., Richard, P.J.H., Ridge, J.C., Ross, M., Roy, M., Seaman, A., Shaw, J., Stea, R.R., Teller, J.T., Thompson, W.B., Thorleifson, L.H., Utting, D.J., Veillette, J.J., Ward, B.C., Weddle, T.K., Wright, H.E., 2020. An updated radiocarbon-based ice margin chronology for the last deglaciation of the North American Ice Sheet Complex. Quat. Sci. Rev. https://doi.org/https://doi.org/10.1016/j.quascirev.2020.106223

Daniels, W.C., Russell, J.M., Giblin, A.E., Welker, J.M., Klein, E.S., Huang, Y., 2017. Hydrogen isotope fractionation in leaf waxes in the Alaskan Arctic tundra. Geochim. Cosmochim. Acta 213, 216–236. https://doi.org/10.1016/j.gca.2017.06.028

Davenport, F.V., Burke, M., Diffenbaugh, N.S., 2021. Contribution of historical precipitation change to US flood damages. Proc. Natl. Acad. Sci. 118, e2017524118. https://doi.org/10.1073/pnas.2017524118

Davtian, N., Bard, E., 2023. A new view on abrupt climate changes and the bipolar seesaw based on paleotemperatures from Iberian Margin sediments. Proc. Natl. Acad. Sci. 120, e2209558120. https://doi.org/10.1073/pnas.2209558120

Dee, S., Emile‐Geay, J., Evans, M.N., Allam, A., Steig, E.J., Thompson, D.M., 2015. PRYSM : An open‐source framework for PRoxY System Modeling, with applications to oxygen‐isotope systems. J. Adv. Model. Earth Syst. 7, 1220–1247. https://doi.org/10.1002/2015MS000447

Diefendorf, A.F., Leslie, A.B., Wing, S.L., 2015. Leaf wax composition and carbon isotopes vary among major conifer groups. Geochim. Cosmochim. Acta 170, 145–156. https://doi.org/10.1016/j.gca.2015.08.018

Easterling, D.R., Kunkel, K.E., Arnold, J.R., Knutson, T., LeGrande, A.N., Leung, L.R., 2017. Precipitation change in the United States, in: Wuebbles, D.J., Fahey, D.W., Hibbard, K.A., Dokken, D.J., Stewart, B.C., Maycock, T.K. (Eds.), Climate Science Special Report: A Sustained Assessment Activity of the U.S. Global Change Research Program. U.S. Global Change Research Program, Washington, D.C., USA, pp. 207–230.

El bani Altuna, N., Ezat, M.M., Smik, L., Muschitiello, F., Belt, S.T., Knies, J., Rasmussen, T.L., 2024. Sea ice-ocean coupling during Heinrich Stadials in the Atlantic–Arctic gateway. Sci. Rep. 14, 1065. https://doi.org/10.1038/s41598-024-51532-7

Fastovich, D., Bhattacharya, T., Jackson, S., Krause, T., Russell, J., Shanahan, T., Sun, C., Williams, J., 2026. Code and Data for Deglacial reconstruction of the spatial extent and intensity of the North Atlantic Subtropical High. https://doi.org/10.5281/ZENODO.20628395

Fastovich, D., Bhattacharya, T., Pérez-Ángel, L.C., Burls, N.J., Feng, R., Knapp, S., Mayer, T., 2024. Large-scale sea surface temperature gradients govern westerly moisture transport in western Ecuador during the Plio-Pleistocene. Earth Planet. Sci. Lett. 640, 118781. https://doi.org/10.1016/j.epsl.2024.118781

Fastovich, D., Russell, J.M., Jackson, S.T., Krause, T.R., Marcott, S.A., Williams, J.W., 2020. Spatial fingerprint of Younger Dryas cooling and warming in eastern North America. Geophys. Res. Lett. 47, e2020GL090031. https://doi.org/https://doi.org/10.1029/2020GL090031

Fastovich, D., Russell, J.M., Marcott, S.A., Williams, J.W., 2022. Spatial fingerprints and mechanisms of precipitation and temperature changes during the Younger Dryas in eastern North America. Quat. Sci. Rev. 294, 107724. https://doi.org/10.1016/j.quascirev.2022.107724

Feakins, S.J., 2013. Pollen-corrected leaf wax D/H reconstructions of northeast African hydrological changes during the late Miocene. Palaeogeogr. Palaeoclimatol. Palaeoecol. 374, 62–71. https://doi.org/10.1016/j.palaeo.2013.01.004

Ficken, K.J., Li, B., Swain, D.L., Eglinton, G., 2000. An *n*-alkane proxy for the sedimentary input of submerged/floating freshwater aquatic macrophytes. Org. Geochem. 31, 745–749. https://doi.org/10.1016/S0146-6380(00)00081-4

Freimuth, E.J., Diefendorf, A.F., Lowell, T.V., Bates, B.R., Schartman, A., Bird, B.W., Landis, J.D., Stewart, A.K., 2020. Contrasting sensitivity of lake sediment n-alkanoic acids and n-alkanes to basin-scale vegetation and regional-scale precipitation δ2H in the Adirondack Mountains, NY (USA). Geochim. Cosmochim. Acta 268, 22–41. https://doi.org/10.1016/j.gca.2019.08.026

Gregoire, L.J., Payne, A.J., Valdes, P.J., 2012. Deglacial rapid sea level rises caused by ice-sheet saddle collapses. Nature 487, 219-U1506. https://doi.org/10.1038/nature11257

Grotjahn, R., 1993. Global atmospheric circulations: observations and theories. Oxford university press, New York Oxford.

Hasanean, H.M., 2004. Variability of the North Atlantic subtropical high and associations with tropical sea-surface temperature. Int. J. Climatol. 24, 945–957. https://doi.org/10.1002/joc.1042

He, C., 2021. Deciphering the Deglacial Evolution of Water Isotope and Climate in the Northern Hemisphere (Ph.D.). ProQuest Diss. Theses. The Ohio State University, United States -- Ohio.

He, F., 2011. Simulating transient climate evolution of the last deglaciation with CCSM 3 (thesis). University of Wisconsin-Madison.

Hersbach, H., Bell, B., Berrisford, P., Hirahara, S., Horányi, A., Muñoz-Sabater, J., Nicolas, J., Peubey, C., Radu, R., Schepers, D., Simmons, A., Soci, C., Abdalla, S., Abellan, X., Balsamo, G., Bechtold, P., Biavati, G., Bidlot, J., Bonavita, M., De Chiara, G., Dahlgren, P., Dee, D., Diamantakis, M., Dragani, R., Flemming, J., Forbes, R., Fuentes, M., Geer, A., Haimberger, L., Healy, S., Hogan, R.J., Hólm, E., Janisková, M., Keeley, S., Laloyaux, P., Lopez, P., Lupu, C., Radnoti, G., de Rosnay, P., Rozum, I., Vamborg, F., Villaume, S., Thépaut, J.-N., 2020. The ERA5 global reanalysis. Q. J. R. Meteorol. Soc. 146, 1999–2049. https://doi.org/10.1002/qj.3803

Hu, J., Emile-Geay, J., Nusbaumer, J., Noone, D., 2018. Impact of Convective Activity on Precipitation δ18O in Isotope-Enabled General Circulation Models. J. Geophys. Res. Atmos. 123, 13,595-13,610. https://doi.org/10.1029/2018JD029187

Ingraham, N.L., Taylor, B.E., 1991. Light stable isotope systematics of large‐scale hydrologic regimes in California and Nevada. Water Resour. Res. 27, 77–90. https://doi.org/10.1029/90WR01708

Ivanovic, R.F., Gregoire, L.J., Burke, A., Wickert, A.D., Valdes, P.J., Ng, H.C., Robinson, L.F., McManus, J.F., Mitrovica, J.X., Lee, L., Dentith, J.E., 2018. Acceleration of Northern Ice Sheet Melt Induces AMOC Slowdown and Northern Cooling in Simulations of the Early Last Deglaciation. Paleoceanogr. Paleoclimatology 33, 807–824. https://doi.org/10.1029/2017pa003308

Jones, R.A., Williams, J.W., Jackson, S.T., 2017. Vegetation history since the last glacial maximum in the Ozark highlands (USA): A new record from Cupola Pond, Missouri. Quat. Sci. Rev. 170, 174–187. https://doi.org/https://doi.org/10.1016/j.quascirev.2017.06.024

Juggins, S., 2013. Quantitative reconstructions in palaeolimnology: new paradigm or sick science? Quat. Sci. Rev. 64, 20–32. https://doi.org/https://doi.org/10.1016/j.quascirev.2012.12.014

Kahmen, A., Dawson, T.E., Vieth, A., Sachse, D., 2011. Leaf wax n-alkane δD values are determined early in the ontogeny of Populus trichocarpa leaves when grown under controlled environmental conditions. Plant Cell Environ. 34, 1639–1651. https://doi.org/10.1111/j.1365-3040.2011.02360.x

Kapsch, M.-L., Mikolajewicz, U., Ziemen, F., Schannwell, C., 2022. Ocean Response in Transient Simulations of the Last Deglaciation Dominated by Underlying Ice-Sheet Reconstruction and Method of Meltwater Distribution. Geophys. Res. Lett. 49, e2021GL096767. https://doi.org/10.1029/2021GL096767

Krause, T.R., Russell, J.M., Zhang, R., Williams, J.W., Jackson, S.T., 2019. Late Quaternary vegetation, climate, and fire history of the Southeast Atlantic Coastal Plain based on a 30,000-yr multi-proxy record from White Pond, South Carolina, USA. Quat. Res. 1–20. https://doi.org/10.1017/qua.2018.95

Li, W., Li, L., Ting, M., Liu, Y., 2012. Intensification of Northern Hemisphere subtropical highs in a warming climate. Nat. Geosci. 5, 830–834. https://doi.org/10.1038/ngeo1590

Liu, Z., Otto-Bliesner, B.L., He, F., Brady, E.C., Tomas, R., Clark, P.U., Carlson, A.E., Lynch-Stieglitz, J., Curry, W., Brook, E., Erickson, D., Jacob, R., Kutzbach, J., Cheng, J., 2009. Transient Simulation of Last Deglaciation with a New Mechanism for Bølling-Allerød Warming. Science 325, 310–314. https://doi.org/10.1126/science.1171041

Marcott, S.A., Bauska, T.K., Buizert, C., Steig, E.J., Rosen, J.L., Cuffey, K.M., Fudge, T.J., Severinghaus, J.P., Ahn, J., Kalk, M.L., McConnell, J.R., Sowers, T., Taylor, K.C., White, J.W.C., Brook, E.J., 2014. Centennial-scale changes in the global carbon cycle during the last deglaciation. Nature 514, 616. https://doi.org/10.1038/nature13799

McGee, D., Moreno-Chamarro, E., Green, B., Marshall, J., Galbraith, E., Bradtmiller, L., 2018. Hemispherically asymmetric trade wind changes as signatures of past ITCZ shifts. Quat. Sci. Rev. 180, 214–228. https://doi.org/10.1016/j.quascirev.2017.11.020

McManus, J.F., Francois, R., Gherardi, J.M., Keigwin, L.D., Brown-Leger, S., 2004. Collapse and rapid resumption of Atlantic meridional circulation linked to deglacial climate changes. Nature 428, 834–837. https://doi.org/10.1038/nature02494

Murphy, A.H., 1988. Skill Scores Based on the Mean Square Error and Their Relationships to the Correlation Coefficient. Mon. Weather Rev. 116, 2417–2424. https://doi.org/10.1175/1520-0493(1988)116%3C2417:SSBOTM%3E2.0.CO;2

Murphy, K., Dee, S., Hancock, C., Pitchon, E., Doss-Gollin, J., Wallace, E., Muñoz, S., 2026. The Changing Relationship Between the Bermuda High, Great Plains Low-Level Jet, and

Mississippi River Basin Hydroclimate From the Last Millennium to 2100. J. Geophys. Res. Atmos. 131, e2025JD044340. https://doi.org/10.1029/2025JD044340
Ortegren, J.T., Knapp, P.A., Maxwell, J.T., Tyminski, W.P., Soulé, P.T., 2011. Ocean–Atmosphere Influences on Low-Frequency Warm-Season Drought Variability in the Gulf Coast and Southeastern United States. J. Appl. Meteorol. Climatol. 50, 1177–1186. https://doi.org/10.1175/2010JAMC2566.1
Otto-Bliesner, B.L., Brady, E.C., Fasullo, J., Jahn, A., Landrum, L., Stevenson, S., Rosenbloom, N., Mai, A., Strand, G., 2016. Climate Variability and Change since 850 CE: An Ensemble Approach with the Community Earth System Model. Bull. Am. Meteorol. Soc. 97, 735–754. https://doi.org/10.1175/BAMS-D-14-00233.1
Otto-Bliesner, B.L., Brady, E.C., Fasullo, J., Jahn, A., Landrum, L., Stevenson, S., Rosenbloom, N., Mai, A., Strand, W., 2025. CESM1 Last Millennium Ensemble 519.812 Tbytes. https://doi.org/10.5065/C32Y-RK84
Otto-Bliesner, B.L., Brady, E.C., Tomas, R., Liu, Z., He, C., 2021. iTraCE. https://doi.org/10.26024/b290-an76
Parnell, A., 2014. Bchron: Radiocarbon dating, age-depth modelling, relative sea level rate estimation, and non-parametric phase modelling. R Package Version 4.
Pausata, F.S.R., Li, C., Wettstein, J.J., Kageyama, M., Nisancioglu, K.H., 2011. The key role of topography in altering North Atlantic atmospheric circulation during the last glacial period. Clim. Past 7, 1089–1101. https://doi.org/10.5194/cp-7-1089-2011
Peltier, W.R., Argus, D.F., Drummond, R., 2015. Space geodesy constrains ice age terminal deglaciation: The global ICE-6G_C (VM5a) model. J. Geophys. Res.-Solid Earth 120, 450–487. https://doi.org/10.1002/2014jb011176
Pendergrass, A.G., Hartmann, D.L., 2014. Changes in the Distribution of Rain Frequency and Intensity in Response to Global Warming. J. Clim. 27, 8372–8383. https://doi.org/10.1175/JCLI-D-14-00183.1
Qiu, W., Collins, M., Scaife, A.A., 2023. Winter Subtropical Highs, the Hadley Circulation and Baroclinic Instability. J. Geophys. Res. Atmos. 128, e2023JD039604. https://doi.org/10.1029/2023JD039604
Rasmusson, E.M., 1967. Atmospheric water vapor transport and the water balance of North America: Part I. Characteristics of the water vapor flux field. Mon. Weather Rev. 95, 403–426. https://doi.org/10.1175/1520-0493(1967)095%3C0403:AWVTAT%3E2.3.CO;2
Robbins, J.A., Edgington, D.N., 1975. Determination of recent sedimentation rates in Lake Michigan using Pb-210 and Cs-137. Geochim. Cosmochim. Acta 39, 285–304. https://doi.org/10.1016/0016-7037(75)90198-2
Rodwell, M.J., Hoskins, B.J., 2001. Subtropical Anticyclones and Summer Monsoons. J. Clim. 14, 3192–3211. https://doi.org/10.1175/1520-0442(2001)014%3C3192:SAASM%3E2.0.CO;2
Rozanski, K., Araguás-Araguás, L., Gonfiantini, R., 1993. Isotopic Patterns in Modern Global Precipitation, in: Climate Change in Continental Isotopic Records. American Geophysical Union (AGU), pp. 1–36. https://doi.org/10.1029/GM078p0001
Sachse, D., Billault, I., Bowen, G.J., Chikaraishi, Y., Dawson, T.E., Feakins, S.J., Freeman, K.H., Magill, C.R., McInerney, F.A., van der Meer, M.T.J., Polissar, P., Robins, R.J., Sachs, J.P., Schmidt, H.L., Sessions, A.L., White, J.W.C., West, J.B., Kahmen, A., 2012. Molecular Paleohydrology: Interpreting the Hydrogen- Isotopic Composition of Lipid Biomarkers from Photosynthesizing Organisms, in: Jeanloz, R. (Ed.), Annual Review of

Earth and Planetary Sciences, Vol 40, Annual Review of Earth and Planetary Sciences. Annual Reviews, Palo Alto, pp. 221–249.
Sachse, D., Dawson, T.E., Kahmen, A., 2015. Seasonal variation of leaf wax n-alkane production and δ2H values from the evergreen oak tree, Quercus agrifolia. Isotopes Environ. Health Stud. 51, 124–142. https://doi.org/10.1080/10256016.2015.1011636
Sachse, D., Gleixner, G., Wilkes, H., Kahmen, A., 2010. Leaf wax *n*-alkane δD values of field-grown barley reflect leaf water δD values at the time of leaf formation. Geochim. Cosmochim. Acta 74, 6741–6750. https://doi.org/10.1016/j.gca.2010.08.033
Saishree, A., Managave, S., Yadava, M.G., Devi, S.M., Sanyal, P., 2024. Tropical Leaf Wax n-Alkane and n-Alkanoic Acid Reflect δD of Precipitation During Early Stages of Leaf Growth: Insights From an Isotope Labeling Experiment. Paleoceanogr. Paleoclimatology 39, e2024PA004899. https://doi.org/10.1029/2024PA004899
Salonen, J.S., Korpela, M., Williams, J.W., Luoto, M., 2019. Machine-learning based reconstructions of primary and secondary climate variables from North American and European fossil pollen data. Sci Rep 9, 13. https://doi.org/10.1038/s41598-019-52293-4
Salonen, J.S., Schenk, F., Williams, J.W., Shuman, B., Lindroth Dauner, A.L., Wagner, S., Jungclaus, J., Zhang, Q., Luoto, M., 2025. Patterns and drivers of Holocene moisture variability in mid-latitude eastern North America. Nat. Commun. 16, 3582. https://doi.org/10.1038/s41467-025-58685-7
Shuman, B.N., Marsicek, J., Oswald, W.W., Foster, D.R., 2019. Predictable hydrological and ecological responses to Holocene North Atlantic variability. Proc. Natl. Acad. Sci. 116, 5985–5990. https://doi.org/10.1073/pnas.1814307116
Song, F., Feng, Z., Leung, L.R., Jr, R.A.H., Wang, J., Hardin, J., Homeyer, C.R., 2019. Contrasting Spring and Summer Large-Scale Environments Associated with Mesoscale Convective Systems over the U.S. Great Plains. J. Clim. 32, 6749–6767. https://doi.org/10.1175/JCLI-D-18-0839.1
Song, F., Leung, L.R., Lu, J., Dong, L., 2018. Future Changes in Seasonality of the North Pacific and North Atlantic Subtropical Highs. Geophys. Res. Lett. 45, 11,959-11,968. https://doi.org/10.1029/2018GL079940
Stahle, D.W., Cleaveland, M.K., 1992. Reconstruction and Analysis of Spring Rainfall over the Southeastern U.S. for the Past 1000 Years. Bull. Am. Meteorol. Soc. 73, 1947–1961. https://doi.org/10.1175/1520-0477(1992)073%3C1947:RAAOSR%3E2.0.CO;2
Stevenson, S., Otto-Bliesner, B.L., Brady, E.C., Nusbaumer, J., Tabor, C., Tomas, R., Noone, D.C., Liu, Z., 2019. Volcanic Eruption Signatures in the Isotope-Enabled Last Millennium Ensemble. Paleoceanogr. Paleoclimatology 34, 1534–1552. https://doi.org/10.1029/2019PA003625
Sun, C., Shanahan, T.M., DiNezio, P.N., McKay, N.P., Roy, P.D., 2021. Great Plains storm intensity since the last glacial controlled by spring surface warming. Nat. Geosci. 14, 912–917. https://doi.org/10.1038/s41561-021-00860-8
Sun, C., Shanahan, T.M., Partin, J., 2019. Controls on the Isotopic Composition of Precipitation in the South-Central United States. J. Geophys. Res. Atmos. 124, 8320–8335. https://doi.org/10.1029/2018JD029306
Teale, N., Robinson, D.A., 2022. Long-term variability in atmospheric moisture transport and relationship with heavy precipitation in the eastern USA. Clim. Change 175, 1. https://doi.org/10.1007/s10584-022-03455-3

Tierney, J.E., Pausata, F.S.R., deMenocal, P.B., 2017. Rainfall regimes of the Green Sahara. Sci. Adv. 3, e1601503. https://doi.org/10.1126/sciadv.1601503

Tierney, J.E., Russell, J.M., Huang, Y.S., Damste, J.S.S., Hopmans, E.C., Cohen, A.S., 2008. Northern hemisphere controls on tropical southeast African climate during the past 60,000 years. Science 322, 252–255. https://doi.org/10.1126/science.1160485

Tipple, B.J., Berke, M.A., Doman, C.E., Khachaturyan, S., Ehleringer, J.R., 2013. Leaf-wax n-alkanes record the plant–water environment at leaf flush. Proc. Natl. Acad. Sci. 110, 2659–2664. https://doi.org/10.1073/pnas.1213875110

Welker, J.M., 2000. Isotopic (δ18O) characteristics of weekly precipitation collected across the USA: an initial analysis with application to water source studies. Hydrol. Process. 14, 1449–1464. https://doi.org/10.1002/1099-1085(20000615)14:8%3C1449::AID-HYP993%3E3.0.CO;2-7

Zhao, J., Gan, T.Y., Zhang, G., Zhang, S., 2023. Projected changes of precipitation extremes in North America using CMIP6 multi-climate model ensembles. J. Hydrol. 621, 129598. https://doi.org/10.1016/j.jhydrol.2023.129598

Zhou, W., Leung, L.R., Song, F., Lu, J., 2021. Future Changes in the Great Plains Low-Level Jet Governed by Seasonally Dependent Pattern Changes in the North Atlantic Subtropical High. Geophys. Res. Lett. 48, e2020GL090356. https://doi.org/10.1029/2020GL090356

Zhou, Y., Lisiecki, L.E., Meyers, S.R., Lee, T., Lawrence, C., 2026. Global and regional Pleistocene benthic $\delta^{18}O$ stacks with a comparison of different age modeling strategies. Geochronology 8, 85–107. https://doi.org/10.5194/gchron-8-85-2026

Zhu, J., Liang, X.-Z., 2013. Impacts of the Bermuda High on Regional Climate and Ozone over the United States. J. Clim. 26, 1018–1032. https://doi.org/10.1175/JCLI-D-12-00168.1

Supplemental Information

Supplemental Text S1. Leaf wax analytical methods and seasonal biases

White Pond sediments were first freeze-dried, homogenized, and all lipid compounds were extracted using a Dionex ASE 350 and a 9:1 mixture of dichloromethane:methanol. The total lipid extract was separated into apolar and polar fractions using alumina columns with 9:1 hexane:dichloromethane and 1:1 dichloromethane:methanol as eluents, respectively (Krause et al., 2019). The apolar fraction was further processed to isolate *n*-alkane leaf waxes. We first added a known quantity of 5α-androstane to aid in quantifying leaf wax biomarkers. We then performed a polarity-based separation using 5% deactivated silica gel columns and eluted with hexane to separate leaf wax *n*-alkanes (apolar alkyl lipids) from mildly polar compounds (e.g. ketone compounds).

The isolated *n*-alkane leaf waxes were quantified using a Thermo TRACE-1310 gas chromatograph with a programmable temperature vaporization inlet and a flame ionization detector. Once quantified, we measured the hydrogen and carbon isotopic composition of C_{31} and C_{27} leaf waxes using a Delta V Plus isotope ratio mass spectrometer in continuous flow mode (Conflo IV) coupled to a Thermo TRACE-1310 through a GC-Isolink II. All samples were measured in duplicate to achieve a precision better than 2‰ for C_{31} δD_{wax} and 0.2‰ for C_{31} $\delta^{13}C_{wax}$. A synthetic *n*-alkane mix (A7 mix from Arndt Schimmelmann at Indiana University) was measured at regular intervals in between samples to monitor instrument drift and correct for any apparent offsets.

Leaf wax biomarkers record the isotopic composition of rainfall during leaf flush for angiosperms and grasses (Daniels et al., 2017; KahmeÂn et al., 2011; Sachse et al., 2015, 2010; Saishree et al., 2024; Tipple et al., 2013). Fossil-pollen abundances at White Pond demonstrate a primarily evergreen conifer assemblage from 21 ka to 10 ka with a large deciduous angiosperm component from 16 to 7 ka (Krause et al., 2019). Since evergreen conifers produce little leaf waxes (Diefendorf et al., 2015; Freimuth et al., 2020), we expect that deciduous angiosperms are the primary leaf wax source at White Pond, which is consistent with $\delta^{13}C_{wax}$ (Figure S2), thereby recording a spring δD_p signal across our record. Prior analyses of Hall's Cave Leaf Area Index indicate that presently leaf flush occurs during the spring which also suggests that Hall's Cave records a springtime δD_p signal (Sun et al., 2021). Because both records reflect springtime precipitation, their difference can be interpreted as a spatial gradient in spring δD_p rather than an artifact of seasonal bias.

Supplemental Text S2. Climate model experimental design

The iTRACE experiments attempt to simulate climate evolution during the last deglaciation with the isotope-enabled Community Earth System Model v1.2 (iCESM). These simulations include transient changes in greenhouse gas concentrations, orbital configuration, ice sheets, and meltwater from 20,000 years before present (ka) to 11 ka. Simulations were performed at a nominal 2° horizontal resolution for the atmosphere and land model and 1° horizontal resolution for the ocean and sea ice models, with 30 vertical layers in the atmosphere.

We compare deglacial iCESM simulations to two additional transient deglacial climate experiments. The TraCE-21ka experiments with CCSM3 (He, 2011; Liu et al., 2009) are the experimental basis for iTRACE and share similar transient changes in greenhouse gas concentrations, orbital configuration, ice sheets, and meltwater from 22 ka to 1950 CE. Experiments with MPI-ESM1-2-CR follow the Paleoclimate Modelling Intercomparison Project Phase 4 LDv1 experimental design (Ivanovic et al., 2016; Kapsch et al., 2022) which has transient updates to orbital configuration, greenhouse gases, ice sheet topography (from ICE-6G_C (Peltier et al., 2015)), and meltwater fluxes consistent with the ice sheet reconstruction. This differs from TraCE-21ka and iTRACE which impose a meltwater forcing designed to reproduce proxy records of the Atlantic Meridional Overturning Circulation which can be as much as two to three times more than global mean sea level rise (Ivanovic et al., 2018). We focus our results on iTRACE but find that our conclusions are insensitive to model choice (Supplemental Text S6). That is, an incomplete characterization of North Atlantic sea surface temperature-North Atlantic Subtropical High-southeastern North American hydroclimate relationship is shared across all models, regardless of the meltwater forcing applied.

iLME, iTRACE, TraCE-21ka, and MPI-ESM1-2-CR do not include simulated integrated vapor transport, which we calculate as:

$$\mathbf{IVT} = \frac{1}{g} \int_{p_{\mathrm{top}}}^{p_{\mathrm{sfc}}} q\,\mathbf{V}\,dp$$

Where **V** is horizontal winds, q is specific humidity, g is gravitational acceleration, p is pressure, p_s is surface pressure, and p_{top} is top of the atmosphere pressure.

Supplemental Text S3. Core-top δD_p estimate at White Pond

We assessed the fidelity of our δD_{wax} measurements at White Pond, SC to record δD_p with a core-top sample. We applied a two-end-member Bayesian mixing model to correct for leaf wax biosynthesis fractionation processes (Tierney et al., 2017), yielding an estimate of δD_p. For C_{31} alkanes, the reconstructed δD_p median estimate is -34.57‰ (95% CI: -40.82, -28.33) while the Online Isotopes in Precipitation Calculator (OIPC) (Bowen, 2025) estimates an annual value of -28.43‰ (p = 0.054, Figure S1). In contrast, the C_{27} the δD_p reconstruction has a median estimate

of -37.36‰ (p = 0.006, 95% CI: -42.77, -31.96). We perform all analyses on C_{31} leaf waxes because the core-top δD_p estimate more closely matches OIPC (Figure S1).

Supplemental Text S4. Reconciling the inverse δD_p gradient-North Atlantic Subtropical High relationship in iTRACE

Unlike evidence from our proxy records, WisoMIP, and iLME, which demonstrate that an intensification and expansion of the North Atlantic Subtropical High increases the zonal $\delta D_p/\delta D_{wax}$ gradient in southeastern North America, the simulated δD_p gradient in iTRACE has an antiphase relationship to the North Atlantic Subtropical High (Figure 3, 4). That is, an increase in the simulated zonal δD_p gradient in southeastern North America occurs when the North Atlantic Subtropical High has weakened and contracted (Figure 3C, S12). Composites comparing intervals of high (≥ 90th percentile) and low (≤ 10th percentile) $\Delta\delta D\ NASH_{iCESM}$ in iTRACE reinforce that the δD_p gradient in southeastern North America is still tied to a large-scale atmospheric reorganization centered on the North Atlantic (Figure 3C, S12). However, periods with a high zonal δD_p gradient in southeastern North America represent time intervals with a northward shift in the Intertropical Convergence Zone (e.g. Bølling-Allerød and Holocene) in response to a resumption of the Atlantic Meridional Overturning Circulation and a subsequent increase in North Atlantic temperature (Figure S13, S14). As the Intertropical Convergence Zone shifts northward following anomalously high temperatures in the North Atlantic (Figure S13, S14), positive precipitation anomalies in the subtropics decrease δDp through the 'amount effect' (Figure S14)(Hu et al., 2018). A northward shift in the Intertropical Convergence Zone also produces easterly integrated vapor transport anomalies in the tropics. These anomalies transmit the negative δD_p signal to Hall's Cave, increasing the zonal δD_p gradient in southeastern North America (Figure 4B, S14). Since the Bølling-Allerød and Holocene represent increases in northern subtropical Atlantic temperatures (Figure S13), the North Atlantic Subtropical High weakens, likely from enhanced atmospheric column thickness over the northern subtropical Atlantic relative to the subpolar North Atlantic (Figure S14). Hence, the erroneous connection between the Intertropical Convergence Zone and Hall's Cave forces an increase in the zonal δD_p gradient in southeastern North America despite a weakening and contraction of the North Atlantic Subtropical High (Figure S12, S15).

Supplemental Text S5. $\Delta\delta D\ NASH_{leaf\ wax}$ uncertainty propagation

We reconstructed variability in the North Atlantic Subtropical High across the last deglaciation using δD_{wax} measurements from White Pond, SC and Hall's Cave, TX and propagated temporal and measurement uncertainties using a Monte Carlo approach. We first generated new Bayesian age models for both sites using *Bacon* (Blaauw and Christen, 2011) and the chronological controls reported in each publication (Krause et al., 2019; Sun et al., 2021). For White Pond, we used the parameters in the original publication (Krause et al., 2019). These parameters were not

recorded for Hall's Cave, so we used the default recommendations from *Bacon*. All *Bacon* parameters and corresponding code are freely available for review (Fastovich et al., 2026). We then defined a common temporal grid for interpolating δD_{wax}, spanning the overlapping age range of both records with a time step equal to the median temporal resolution across both sites.

To generate an ensemble of interpolated δD_{wax} records, we first propagated measurement uncertainty by randomly resampling δD_{wax} from $N\left(\mu_{\mathrm{wax}}, \frac{\sigma_{\mathrm{wax}}}{\sqrt{N}}\right)$, where $N = 2$, reflecting duplicate measurements at both sites. At White Pond, μ_{wax} and σ_{wax} were estimated from the duplicate measurements directly. Individual σ_{wax} values were not reported for Hall's Cave, so we assigned $\sigma_{\mathrm{wax}} = 5$ based on measurement uncertainties described in the original publication and assume that reported δD_{wax} values estimate μ_{wax} (Sun et al., 2021). Each resampled δD_{wax} record was then interpolated to the common temporal grid using age estimates drawn randomly from the posterior ensemble of the *Bacon* age models. Repeating this process 1,000 times produced an ensemble of interpolated δD_{wax} records that incorporate both age and measurement uncertainties. We standardized each ensemble member and subtracted the Hall's Cave ensemble from the White Pond ensemble, yielding 1,000 estimates of $\Delta\delta D\ NASH_{leaf\ wax}$, from which we report the median and 95% confidence interval.

Supplemental Text S6. Bermuda High Index sensitivity tests

Many index-based formulations have been proposed to examine the strength of the North Atlantic Subtropical High (Ortegren et al., 2011; Song et al., 2018; Stahle and Cleaveland, 1992; Zhu and Liang, 2013). All indices but the Zhu and Liang (2013) index in TraCE-21ka and iTRACE share common millennial-scale climate variability and identify that changes in the Atlantic Meridional Overturning Circulation are an important control on the North Atlantic Subtropical High, regardless of index choice (18 to 15 ka and 13 to 12 ka in iTRACE, 18 to 15 ka and 14.5 to 14 ka in TraCE-21ka, 14.6 to 13.6 ka and 13 to 12.2 ka in MPI-ESM1-2-CR, Figure S8, S9, S10). In addition, trends across the last deglaciation are sensitive to the Bermuda High Index selected. Only indices that are designed to track central North Atlantic Subtropical High pressures (Murphy et al., 2026) indicate a weakening of the North Atlantic Subtropical High from 21 ka to 11 ka (Figure S8, S9, S10) (MCP in Ortegren et al., 2011; Song et al., 2018), aligning with increases in sea surface temperatures and decreasing $\Delta\delta D\ NASH_{leaf\ wax}$ from 15 ka to 10 ka (Figure 2). In contrast, indices that compare mean sea level pressure from southeastern North America or the central United States to the North Atlantic (i.e. the zonal sea level pressure gradient) demonstrate either a marginal (BHI in Ortegren et al., 2011; Stahle and Cleaveland, 1992) or a large *increase* in index values (Zhu and Liang, 2013) which produce conflicting interpretations of North Atlantic Subtropical High variability.

Common millennial scale variability and trends between all gradient based indices (Ortegren et al., 2011; Stahle and Cleaveland, 1992; Zhu and Liang, 2013) are unexpected and identifies a key limitation across models. Mean sea level pressure near/in the Gulf of Mexico is in all four indices but with opposite signs (North Atlantic - Gulf of Mexico in Ortegren et al. (2011) and Stahle and Cleaveland with (1992) and Gulf of Mexico - Great Plains in Zhu and Liang (2013) and our modified version of Zhu and Liang (2013)) which should produce anticorrelated patterns across the last deglaciation. Positive values the Zhu and Liang (2013) and our modified index are associated with a westward expanded North Atlantic Subtropical High whereas positive values in the Bermuda High Index in Ortegren et al. (2011) and Stahle and Cleaveland (1992) are associated with an eastward location of the North Atlantic Subtropical High western flank (Murphy et al., 2026). Therefore, a common increase in all gradient based indices during periods of meltwater addition and across the entire last deglaciation leads to the contradictory conclusion that the North Atlantic Subtropical High expanded westward and the North Atlantic Subtropical High western flank shifted eastward. An inferred eastward shift in the core of North Atlantic Subtropical High and a westward expansion of the flank may partially resolve this contradiction but no Bermuda High Index tracks the migration of the North Atlantic Subtropical High and its extent simultaneously.

We proceed with the Zhu and Liang (2013) index because of our site locations: Hall's Cave is in the Southern Great Plains region and this index was explicitly developed to track the influence of the North Atlantic Subtropical High on regional climates in the United States. Meanwhile, all gradient-based indices only consider mean sea level pressure in the Gulf of Mexico (mean sea level pressure in New Orleans corresponds to the Gulf of Mexico in Ortegren et al., 2011; Stahle and Cleaveland, 1992) and aim to capture general features of the North Atlantic Subtropical High, not how it influences the southeastern North American hydroclimate (Zhu and Liang, 2013). However, we shift the Gulf of Mexico region ten degrees to the east because deglacial boundary conditions in the transient, deglacial simulations shift the mean position of the North Atlantic Subtropical High. Additionally, we standardize mean sea level pressure in the Great Plains and the Gulf of Mexico before differencing because glacial cooling raises mean sea level pressure across both regions (the hypsometric effect), and this shared trend overwhelms changes in the North Atlantic Subtropical High position (Figure S16). Standardizing before differencing weights both regions equally, so the common signal largely cancels and positional changes remain. In TraCE-21ka and MPI-ESM1-2-CR we find that our modifications and the original Zhu and Liang (2013) index produce the same conclusion as in iTRACE: a westward expanded North Atlantic Subtropical High is associated with increased moisture transport at White Pond, not at Hall's Cave as expected from ERA5 analyses (Figure 1, S8, S9, S10, S16). In iTRACE, the original Zhu and Liang (2013) index does not exhibit millennial-scale climate variability while our modified index does. We hypothesize that this may be related to iCESM-specific mean state biases in the longitudinal position of the North Atlantic Subtropical High.

Supplemental Text S7. Pseudoproxy reconstruction of the North Atlantic Subtropical High

We examine the ability of leaf wax biomarkers at White Pond and Hall's Cave to reconstruct changes in the North Atlantic Subtropical High through a pseudoproxy approach that simulates *n*-alkane synthesis, burial, bioturbation, and corresponding measurement and temporal uncertainties. We use PRYSM (Dee et al., 2015) for all proxy system modeling at White Pond and Hall's Cave with simulated δD_p from iTRACE for the four grid cells surrounding each site as the input into our leaf wax sensor model. PRYSM includes a leaf wax sensor model, an archive model to simulate sedimentation and sediment compaction, a bioturbation model, and an observation model. The observation model encompasses sediment subsampling, radiocarbon dating, age-depth modeling, and analytical error (Dee et al., 2015). Together, these models produce an ensemble (1,000) of pseudoproxy estimates of δD_{wax} at White Pond and Hall's Cave. We take the same analytical procedure to estimate $\Delta\delta D\ NASH_{pseudoproxy}$ as for $\Delta\delta D\ NASH_{leaf\ wax}$. That is, we take the standardized difference of $\delta D_{pseudoproxy}$ between White Pond and Hall's Cave in a Monte Carlo resampling framework to propagate temporal and measurement uncertainty and calculate $\Delta\delta D\ NASH_{pseudoproxy}$, a direct pseudoproxy analog to $\Delta\delta D\ NASH_{leaf\ wax}$.

We modified the parameters in each PRYSM submodel to mimic the unique site-specific characteristics at both sites. For White Pond, the leaf wax sensor model was given empirical estimates of C_3 and C_4 apparent fractionation values from Sachse et al., (2012) for C_{31} alkanes and propagated apparent fractionation measurement uncertainty. We use White Pond fossil-pollen observations (Krause et al., 2019) and $C_{31}\ \delta^{13}C_{wax}$ to set an initial C_4 fraction of 10% and allow this fraction to evolve following an Ornstein-Uhlenbeck (OU) process (Figure S2). This conservative analytical choice reduces the sensitivity of our leaf wax sensor model because fossil-pollen observations indicate that grass pollen abundance never increases beyond 10%, but the OU process can exceed that. For the archive model we use default PRYSM porosity values and a sedimentation rate of 13 cm/ka, based on the calculated sedimentation rate at White Pond (Dee et al., 2015; Krause et al., 2019). For the bioturbation model we choose a mixed layer-depth of 5 cm, aligning with estimates from eastern North American lakes (Robbins and Edgington, 1975). For the observation model, we propagate temporal uncertainty by generating an ensemble of age-depth estimates using *Bchron* (Parnell, 2014) with synthetic radiocarbon ages at the same temporal positions as in the White Pond sedimentary profile. Synthetic radiocarbon ages at identical positions as in White Pond were generated by taking the true age of the simulated proxy system model core, calculating the corresponding radiocarbon age, and adding radiocarbon measurement uncertainty that was 10% of the radiocarbon age. We additionally subsample the simulated sedimentary archive in the same positions as White Pond. Lastly, we simulate C_{31} alkanes measurement uncertainty by adding white noise that matches our target standard deviation of 2‰ across two replicates for White Pond δD_{wax} measurements. An identical procedure was followed at Hall's Cave, but with parameters updated reflecting site-specific

factors (i.e. C_{27} leaf wax sensor model, more radiocarbon ages, more subsamples). We direct the reader to our Zenodo repository (script hc_pseudoproxy.py) for exact parameter estimates (Fastovich et al., 2026). Though the PRYSM lake sediment model is an imperfect approach for Hall's Cave, no proxy system model exists for cave sediments and our approach still offers a first-order approximation of δD_{wax} uncertainties.

We assess the ability of $\Delta\delta D\ NASH_{pseudoproxy}$ to predict variability in southeastern North American meridional integrated vapor transport, Bermuda High Index, and North Atlantic sea surface temperatures with the coefficient of efficiency (CE) using leave-one-block-out cross-validation and composites. The input record is divided into three blocks of equal sample size and each block is verified against a regression calibrated on the remaining blocks. All time series are linearly detrended within each block before calibration, and CE is decomposed (Murphy, 1988) to diagnose the sources of high or low skill. We assess the predictive skill of $\Delta\delta D\ NASH_{iCESM}$ to estimate southeast North American meridional integrated vapor transport, Bermuda High Index, and North Atlantic sea surface temperatures which sets an upper limit (i.e. our pseudoproxy estimates cannot outperform iTRACE simulated δD_p used as an input into the proxy system model). We then calculate CE for the median $\Delta\delta D\ NASH_{pseudoproxy}$ estimate and then on each $\Delta\delta D\ NASH_{pseudoproxy}$ ensemble member and compare all predictive skills to random walk surrogates. If our pseudoproxy $\Delta\delta D\ NASH_{pseudoproxy}$ has predictive skill comparable to $\Delta\delta D\ NASH_{iCESM}$, we conclude that our proxy-based $\Delta\delta D\ NASH_{leaf\ wax}$ index is recording upstream variability in the North Atlantic Subtropical High, mediated through changes in meridional integrated vapor transport. Notably, $\Delta\delta D\ NASH_{pseudoproxy}$ is insensitive to climate model biases inherent in iTRACE because the simulated δD_p inputs into our pseudoproxy model are from iTRACE.

We find that in all cases $\Delta\delta D\ NASH_{pseudoproxy}$ is less predictive than $\Delta\delta D\ NASH_{iCESM}$ but is still sensitive to atmospheric reorganization in the North Atlantic. Composites based on $\Delta\delta D\ NASH_{pseudoproxy}$ and $\Delta\delta D\ NASH_{iCESM}$ return the same spatial changes in δD_p, the 1030 mb contour, and integrated vapor transport (Figure S17). Within southeastern North America, integrated vapor transport composites exhibit southerly flow in the $\Delta\delta D\ NASH_{pseudoproxy}$ and $\Delta\delta D\ NASH_{iCESM}$ composites (Figure S17). Similarly, over the Gulf of Mexico $\Delta\delta D\ NASH_{pseudoproxy}$ and $\Delta\delta D\ NASH_{iCESM}$ composites demonstrate a strong easterly component (Figure S17). δD_p composites over eastern North America are negative in the $\Delta\delta D\ NASH_{pseudoproxy}$ and $\Delta\delta D\ NASH_{iCESM}$ composites with a similar magnitude between -4 and -10‰. Mean sea level pressure in the low and high $\Delta\delta D\ NASH_{pseudoproxy}$ and $\Delta\delta D\ NASH_{iCESM}$ composites show high agreement. The high composite in (pink line in Figure S17) $\Delta\delta D\ NASH_{pseudoproxy}$ and $\Delta\delta D\ NASH_{iCESM}$ are both smaller than the low composite (gray line in Figure S17). Collectively, results suggest that $\Delta\delta D\ NASH_{pseudoproxy}$ is able to capture atmospheric circulation reorganization upstream of southeastern North America that is linked to variability in North Atlantic sea surface temperatures.

Quantitative skill estimates show that the $\Delta\delta D\ NASH_{pseudoproxy}$ predicts southeast North American meridional integrated vapor transport, the Bermuda High Index, and North Atlantic sea surface temperatures, although degradation introduced by PRYSM reduces this skill relative to the undegraded $\Delta\delta D\ NASH_{iCESM}$. For the Bermuda High Index, $\Delta\delta D\ NASH_{iCESM}$ has a CE between 0.22 and 0.64 across the three blocks and defines the upper predictive limit. We find that the median of the $\Delta\delta D\ NASH_{pseudoproxy}$ ensemble has a CE of ~0 across all blocks, implying no predictive skill (Figure S18D). However, CE decomposition identifies that the Bermuda High Index predicted from a linear model fit on the median $\Delta\delta D\ NASH_{pseudoproxy}$ estimate has a Pearson correlation between 0.22 and 0.35 indicating some correspondence between predicted Bermuda High Index values and true values (Figure S18G). Therefore, the ~0 CE values for the ability of $\Delta\delta D\ NASH_{pseudoproxy}$ to predict the Bermuda High Index is attributed to the difference in the variability between $\Delta\delta D\ NASH_{pseudoproxy}$ predicted Bermuda High Index values and true values. Indeed, in the 20 to 17 ka and the 14 to 11 ka block, the standard deviation ratio for the median $\Delta\delta D\ NASH_{pseudoproxy}$ predictor is 0.25 and 0.07, respectively (Figure S18J). Meanwhile, these blocks have a standard deviation ratio of 0.59 and 0.83 when $\Delta\delta D\ NASH_{iCESM}$ is used as the predictor (Figure S18). Collectively, the moderate correlations (Figure S18G), low standard deviation ratios (Figure S18J), and ~0 CE (Figure S18D) indicate that the median $\Delta\delta D\ NASH_{pseudoproxy}$ is predictive of the timing of changes in the Bermuda High Index, but struggles to correctly predict amplitude. This interpretation aligns with a visual assessment of the individual time series (Figure S18).

Though the median of the $\Delta\delta D\ NASH_{pseudoproxy}$ ensemble has some predictive skill, individual $\Delta\delta D\ NASH_{pseudoproxy}$ ensemble members struggle to accurately predict the timing and amplitude of the Bermuda High Index. Only 25% of the $\Delta\delta D\ NASH_{pseudoproxy}$ ensemble members have a Pearson correlation between predicted and true Bermuda High Index values greater than median $\Delta\delta D\ NASH_{pseudoproxy}$ (Figure S18G). Each $\Delta\delta D\ NASH_{pseudoproxy}$ ensemble member includes an age-depth relationship that is drawn at random from the posterior distribution of the simulated White Pond and Hall's Cave $\delta D_{pseudoproxy}$. Changes in the timing of key increases and decreases in $\Delta\delta D\ NASH_{pseudoproxy}$ ensemble members lead to a misalignment with the Bermuda High Index and poor predictive skill (Figure S18A). A potentially large cause of the poor predictive skill of individual $\Delta\delta D\ NASH_{pseudoproxy}$ ensemble members are biases in simulated δD_p. δD_{wax} at White Pond decreases by ~25‰ from 21 ka to 10.5 ka while simulated δD_p only increases by ~10‰ (Figure S7), yet we apply the same analytical uncertainty as our true δD_{wax} measurements. If simulated δD_p is underestimated across the last deglaciation, our addition of analytical noise based on true White Pond and Hall's Cave measurements greatly reduces the signal to noise ratio, reducing the predictive ability of any individual $\Delta\delta D\ NASH_{pseudoproxy}$ ensemble member. This may explain why $\Delta\delta D\ NASH_{pseudoproxy}$ has a larger 95% confidence interval than $\Delta\delta D\ NASH_{leaf\ wax}$ for which we also propagate temporal and analytical uncertainty (Figure 2, S18A). This also explains why the median of the $\Delta\delta D\ NASH_{pseudoproxy}$ ensemble has some predictive skill; when taking the median the added measurement noise somewhat cancels out and the

underlying signal emerges. If poor predictability for individual $\Delta\delta D\ NASH_{pseudoproxy}$ ensemble members is an issue of temporal uncertainty, taking the median of the $\Delta\delta D\ NASH_{pseudoproxy}$ ensemble would have a similar effect by averaging across misaligned ensemble members to produce a median $\Delta\delta D\ NASH_{pseudoproxy}$ that is aligned with the Bermuda High Index.

$\Delta\delta D\ NASH_{pseudoproxy}$ has more predictive skill for southeastern North American meridional integrated vapor transport and North Atlantic sea surface temperatures with CE results that mirror the Bermuda High Index. CE is ~0 across all blocks with high Pearson correlations between predicted and observed values for southeastern North American meridional integrated vapor transport and North Atlantic sea surface temperatures when examining the median of the $\Delta\delta D\ NASH_{pseudoproxy}$ ensemble (Figure S18H, S18I). As with the Bermuda High Index, low CE but high Pearson correlations indicate that the $\Delta\delta D\ NASH_{pseudoproxy}$ ensemble median correctly captures the timing of changes in southeastern North American meridional integrated vapor transport and North Atlantic sea surface temperatures but struggles to predict the correct amplitude (Figure S18H, S18K, S18I, S18L). Individual ensemble members also have less predictive skill than the $\Delta\delta D\ NASH_{pseudoproxy}$ ensemble median as in the Bermuda High Index (Figure S18E, S18F).

Lastly, the temporal evolution of $\Delta\delta D\ NASH_{pseudoproxy}$ closely mirrors $\Delta\delta D\ NASH_{iCESM}$ and all predictive targets (Bermuda High Index, southeastern North American meridional integrated vapor transport, North Atlantic sea surface temperatures) but with muted variability and a slight temporal offset caused by the bioturbation PRYSM submodel (Figure S17A, S17B, S18A-C). Bioturbation smooths the higher-frequency variability in $\Delta\delta D\ NASH_{pseudoproxy}$, which is expected to reduce predictive skill. Within each calibration block, the variability available for training is largely at these high frequencies, so the linear model cannot learn the true relationship between $\Delta\delta D\ NASH_{pseudoproxy}$ and the target, resulting in low CE values in the verification block. Since CE is evaluated within each verification block, it does not credit the ability of $\Delta\delta D\ NASH_{pseudoproxy}$ to capture changes between blocks (i.e. millennial-scale variability). Nevertheless, millennial-scale variability present in both $\Delta\delta D\ NASH_{pseudoproxy}$ and $\Delta\delta D\ NASH_{iCESM}$ are a product of the large forcings applied in iTRACE, which produce a δD_p signal that survives the noise introduced by PRYSM and support our use of $\Delta\delta D\ NASH_{leaf\ wax}$ at millennial timescales.

Supplemental Figures

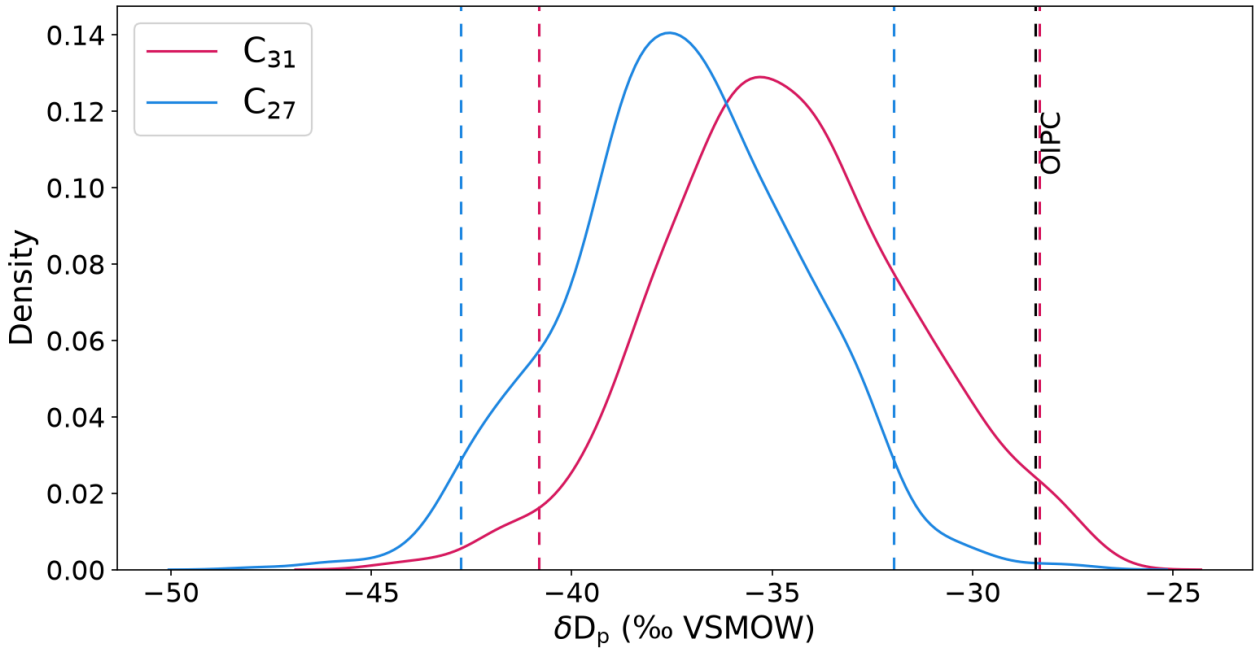


Figure S1. The posterior distribution of predicted δD_p for core top sediment from White Pond where predictions are from a two-end member Bayesian mixing model (Tierney et al., 2017). δD_p was reconstructed for C_{31} and C_{27} leaf waxes, with C_{31} showing a closer agreement to observations from the Online Isotopes in Precipitation Calculator. The colored dashed lines correspond to the 95% confidence interval for reconstructed δD_p. The second dashed line near -28‰ for C_{31} is near the black dashed line. The black dashed line corresponds to δD_p for the closest grid cell to White Pond from the Online Isotopes in Precipitation Calculator (Bowen, 2025).

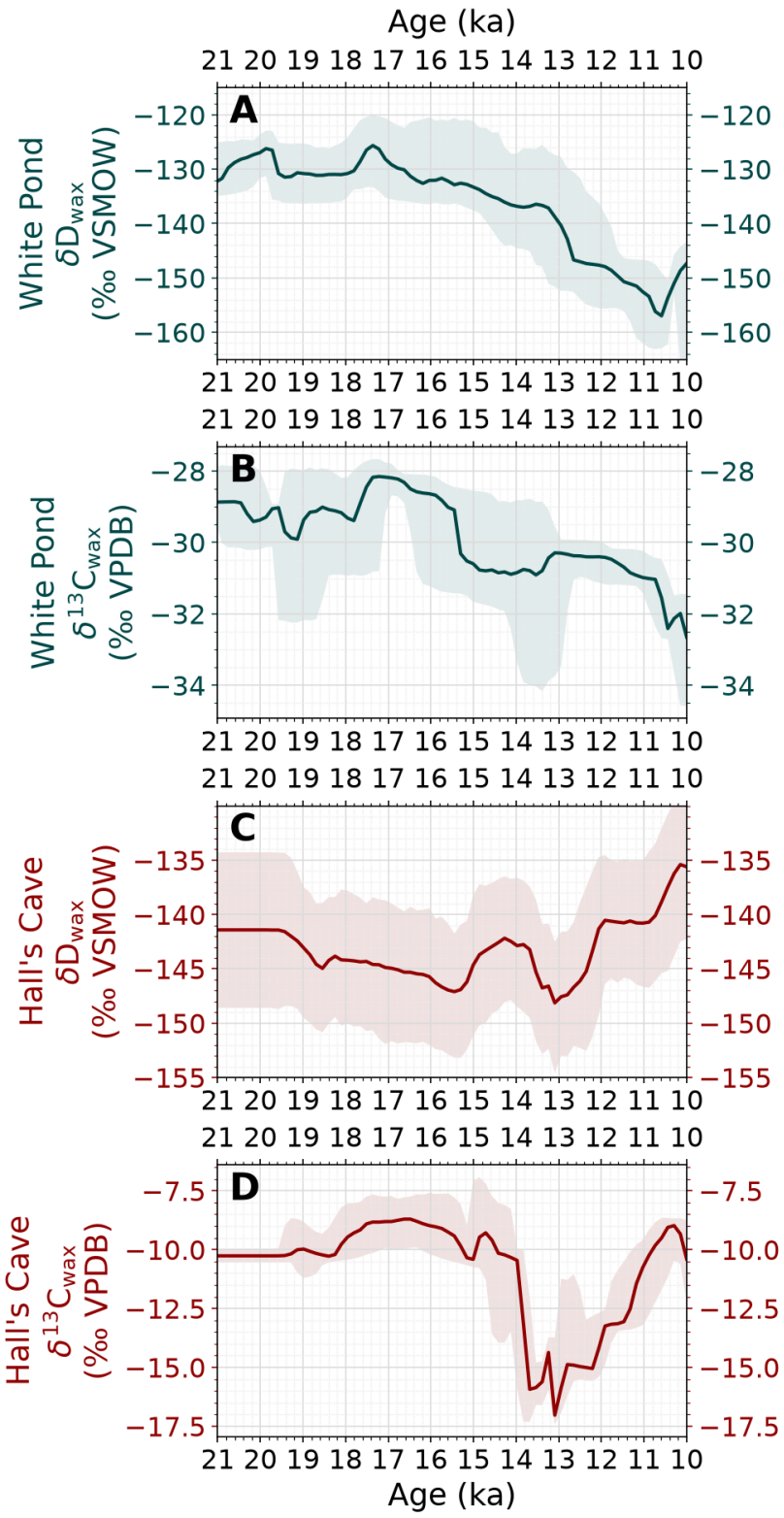


Figure S2. Median White Pond (A) δD_{wax} and (B) $\delta^{13}C_{wax}$ (green shading represents the 95% CI) from a resampling approach that propagates measurement and temporal uncertainty. Median Hall's Cave (C) δD_{wax} and (D) $\delta^{13}C_{wax}$ (green shading represents the 95% CI) from a resampling approach that propagates measurement and temporal uncertainty.

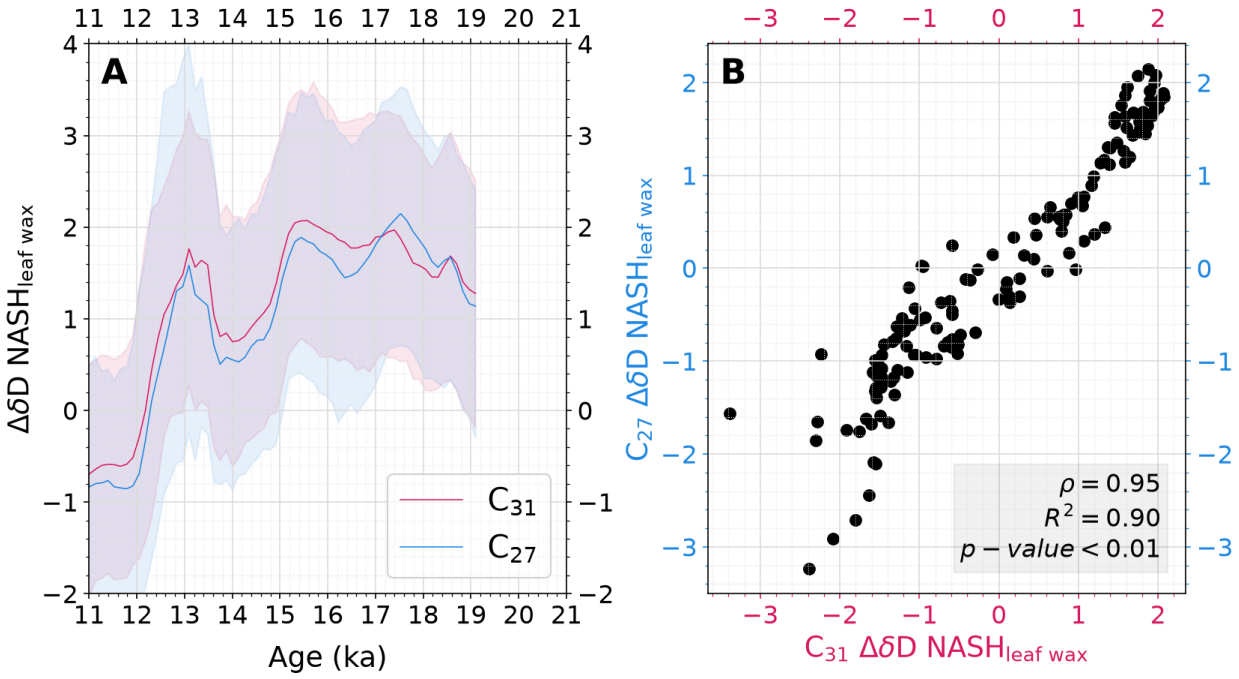


Figure S3. (A) A comparison of North Atlantic Subtropical High reconstructions using C_{31} (pink) and C_{27} (blue) chain length alkanes from White Pond and C_{27} alkanes from Hall's Cave. (B) A crossplot of paired North Atlantic Subtropical High reconstructions from (A). Note the high similarity between reconstructions and high correlation. This suggests that our North Atlantic Subtropical High reconstruction is not sensitive to our analytical decision to focus on C_{31} alkanes at White Pond.

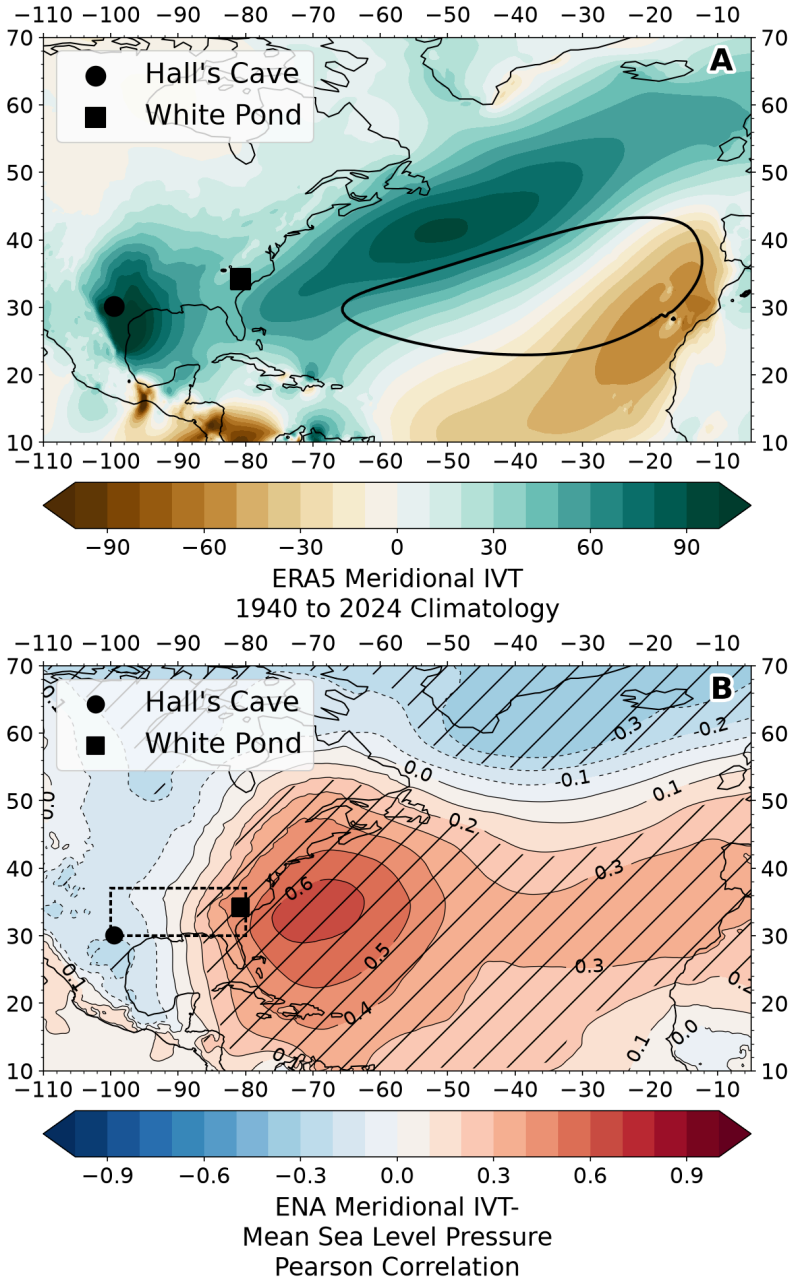


Figure S4. (A) The 1940 to 2024 climatology of meridional integrated vapor transport in southeastern North America and the 1019 hPa isobar (black contour) from ERA5. (B) The Pearson correlation between meridional integrated vapor transport into southeastern North America (black dashed box) and mean sea level pressure. Regions with significant correlations are denoted with hashing. Significant correlations over the Atlantic suggest that the geostrophic balance between the North Atlantic Subtropical High and low pressure over eastern North America drive meridional moisture flux into southeastern North America.

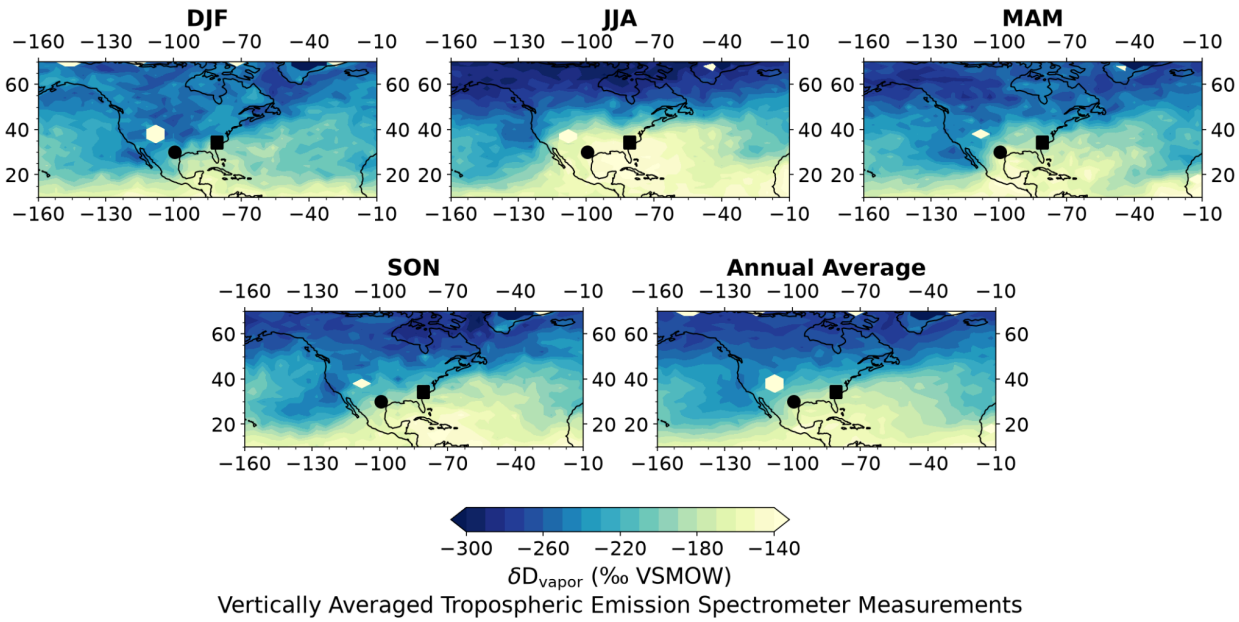


Figure S5. Seasonal and annual climatology of δD_{vapor} from the Tropospheric Emission Spectrometer (TES). Estimates are pressure-weighted and averaged between 825 and 450 hPa. The square and circle points correspond to White Pond and Hall's Cave, respectively. Post-processed data is from (Fastovich et al., 2024).

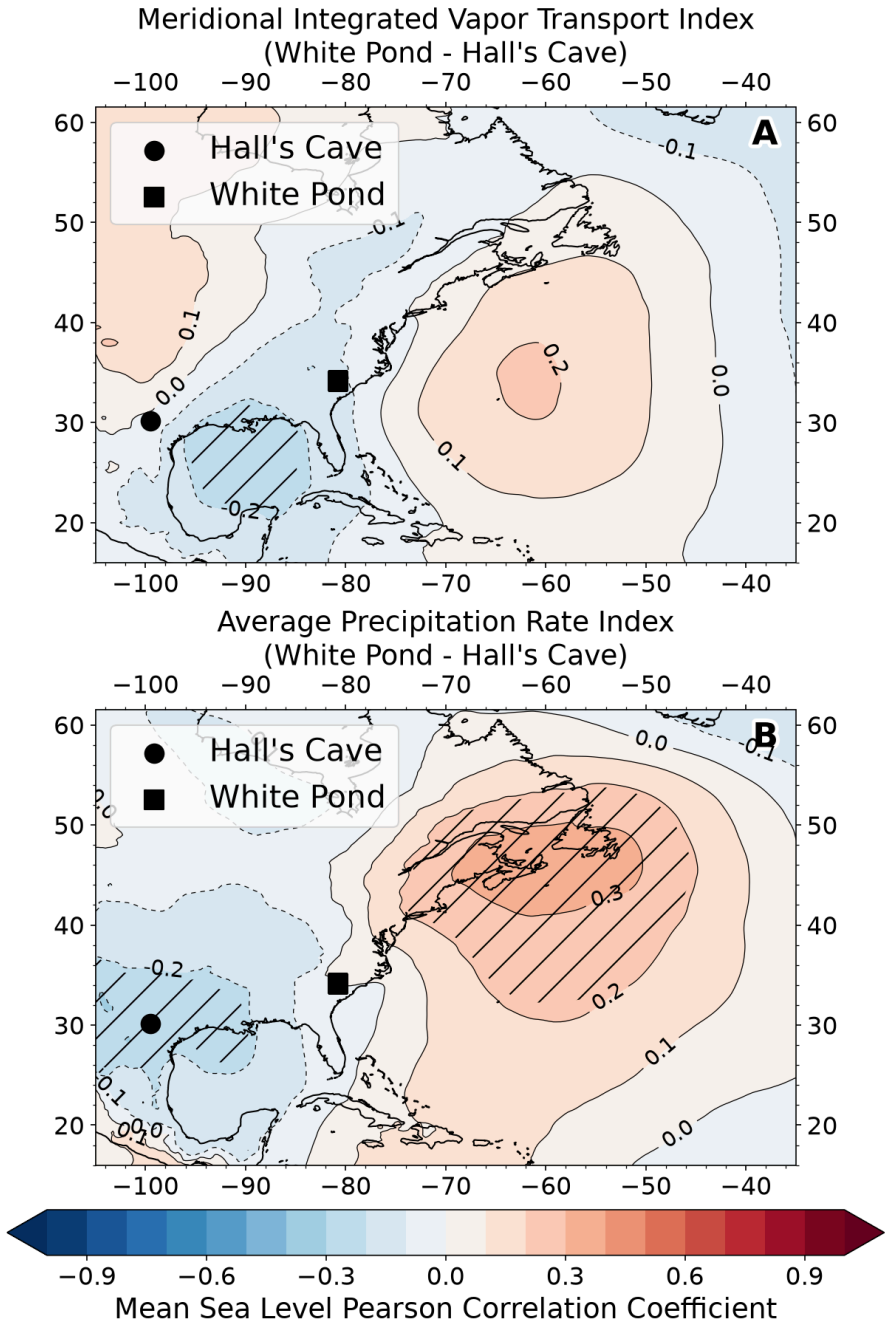


Figure S6. (A, B) The filled contours correspond to the Pearson correlation between indices that replicate ΔδD NASH, but with meteorological fields from ERA5. (A) The standardized difference between meridional integrated vapor transport at White Pond and Hall's Cave is compared to mean sea level pressure. Regions with significant correlations are denoted with hashing. Significant correlations over the Gulf of Mexico suggest that westward expansions in the North Atlantic Subtropical High are correlated with the difference in meridional integrated vapor transport between our two sites. (B) The standardized difference between average precipitation rate at White Pond and Hall's Cave is compared to mean sea level pressure. Regions with significant correlations are denoted with hashing. Significant correlations over the Atlantic suggest that the intensity of the North Atlantic Subtropical High is correlated with the difference in average precipitation rate between our two sites.

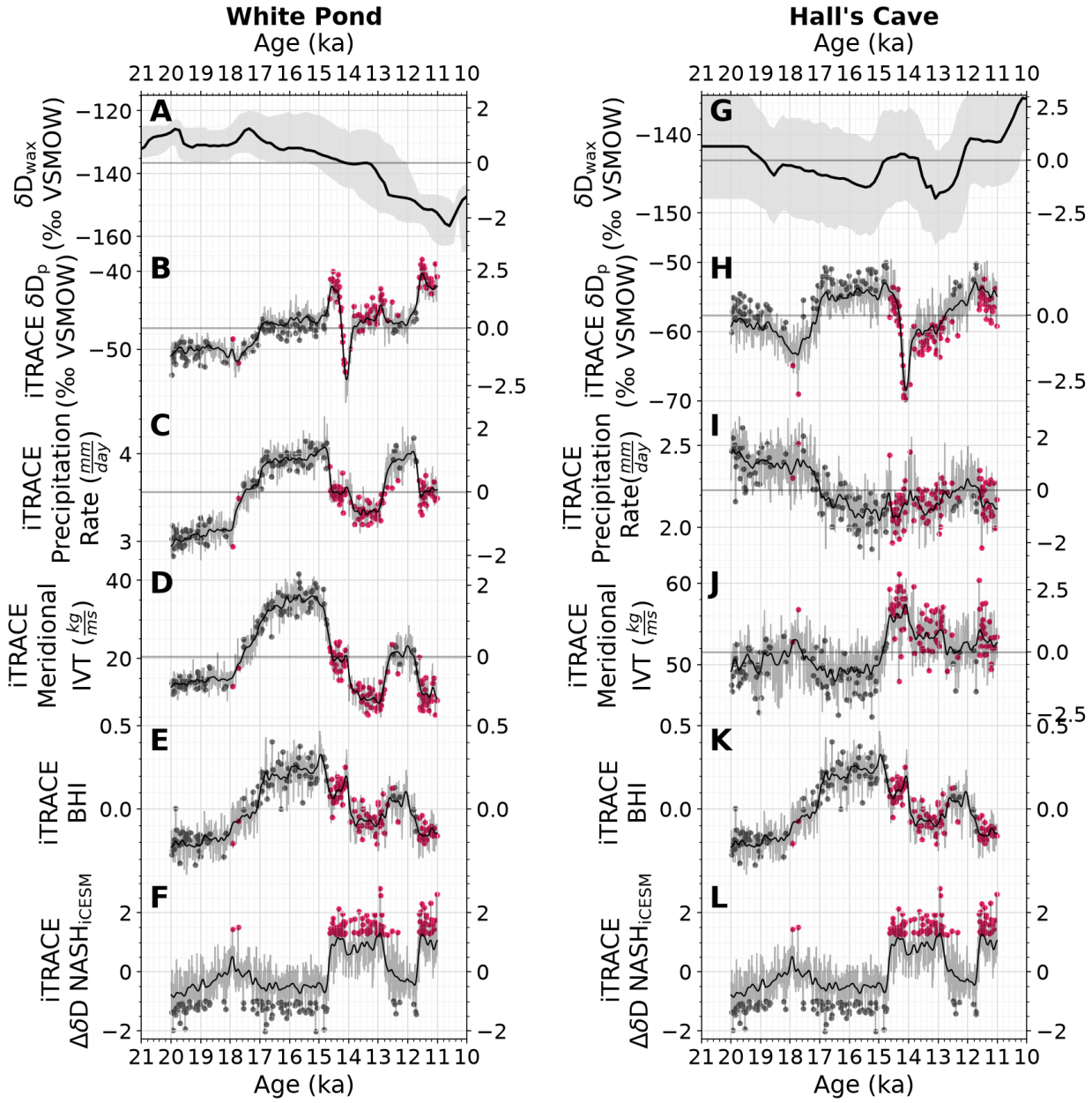


Figure S7. Measured δD_{wax} from (A) White Pond and (G) Hall's Cave with temporal and measurement uncertainty propagated through a resampling approach compared to simulated, iTRACE, time series of site-level (B, H) δD_p, (C, I) precipitation rate, and (D, J) meridional integrated vapor transport. (E, K) Simulated BHI from iTRACE. (F, L) $\Delta\delta D\ NASH_{iCESM}$ calculated identically to $\Delta\delta D\ NASH_{leaf\ wax}$. In all iTRACE panels (B-F, H-L), the pink points correspond to time periods when $\Delta\delta D\ NASH_{iCESM} \geq$ 90th percentile. The gray points correspond to time periods when $\Delta\delta D\ NASH_{iCESM} \leq$ 10th percentile. Except for (A) and (G), the light gray line corresponds to decadal averages and the dark lines correspond to a Gaussian low-pass filter (σ = 50 years). In A-D and G-J, the right y-axis corresponds to standardized values with the horizontal line representing standardized values of 0.

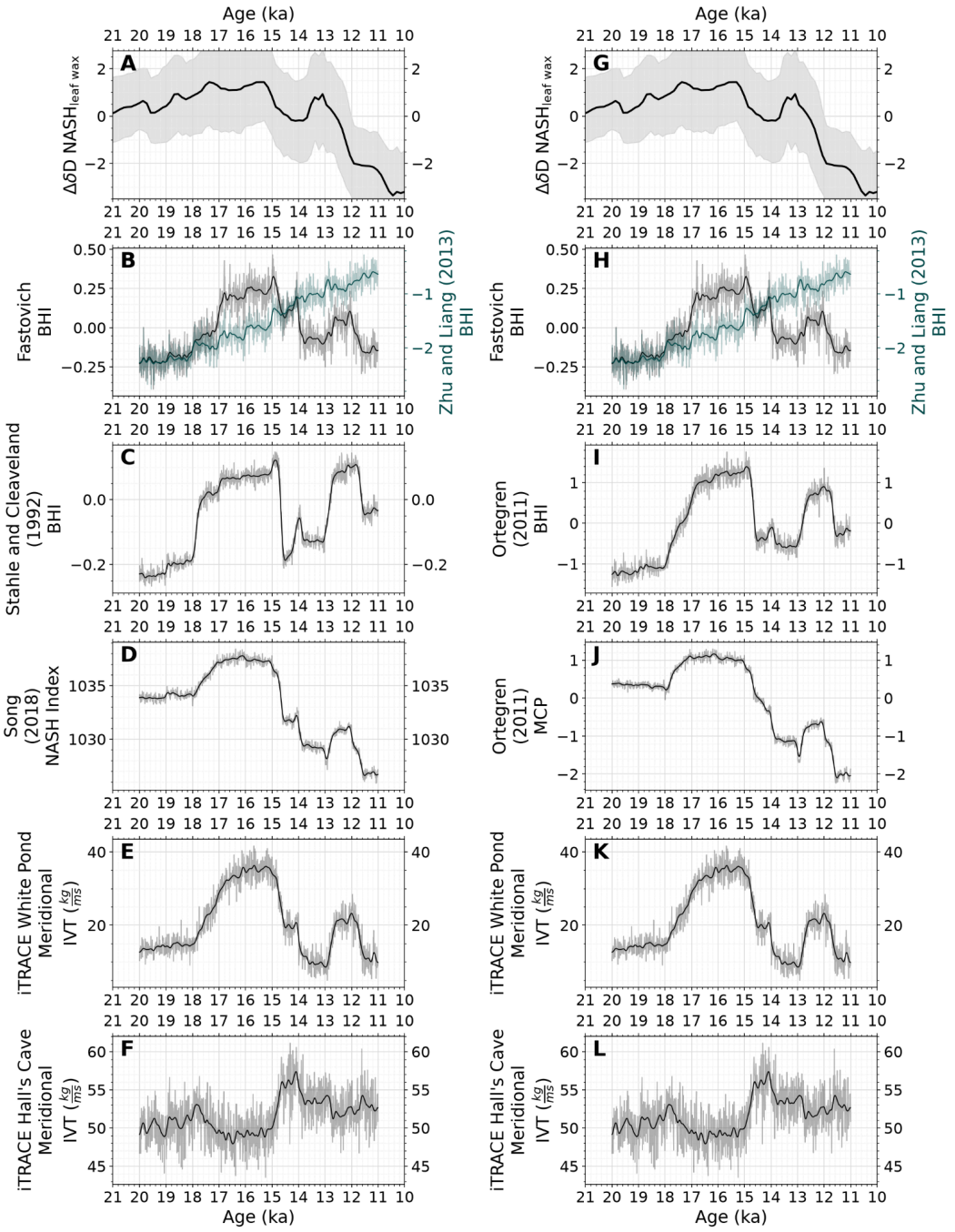


Figure S8. Alternative Bermuda High Index formulations from (B) Zhu and Liang (green line) (2013), (C) Stahle and Cleaveland (1992), (D) Song et al., (2018) (I) Ortegren et al., (2011), (J) mean central pressure index from Ortegren et al., (2011) for iTRACE. These indices are compared to the index used here (black line in B, H), integrated vapor transport at (E, K) White Pond and (F, L) Hall's Cave, and (A, G) $\Delta\delta D\ NASH_{leaf\ wax}$. In all panels except A and G, the light lines correspond to decadal averages and the dark lines correspond to a Gaussian low-pass filter (σ = 50 years).

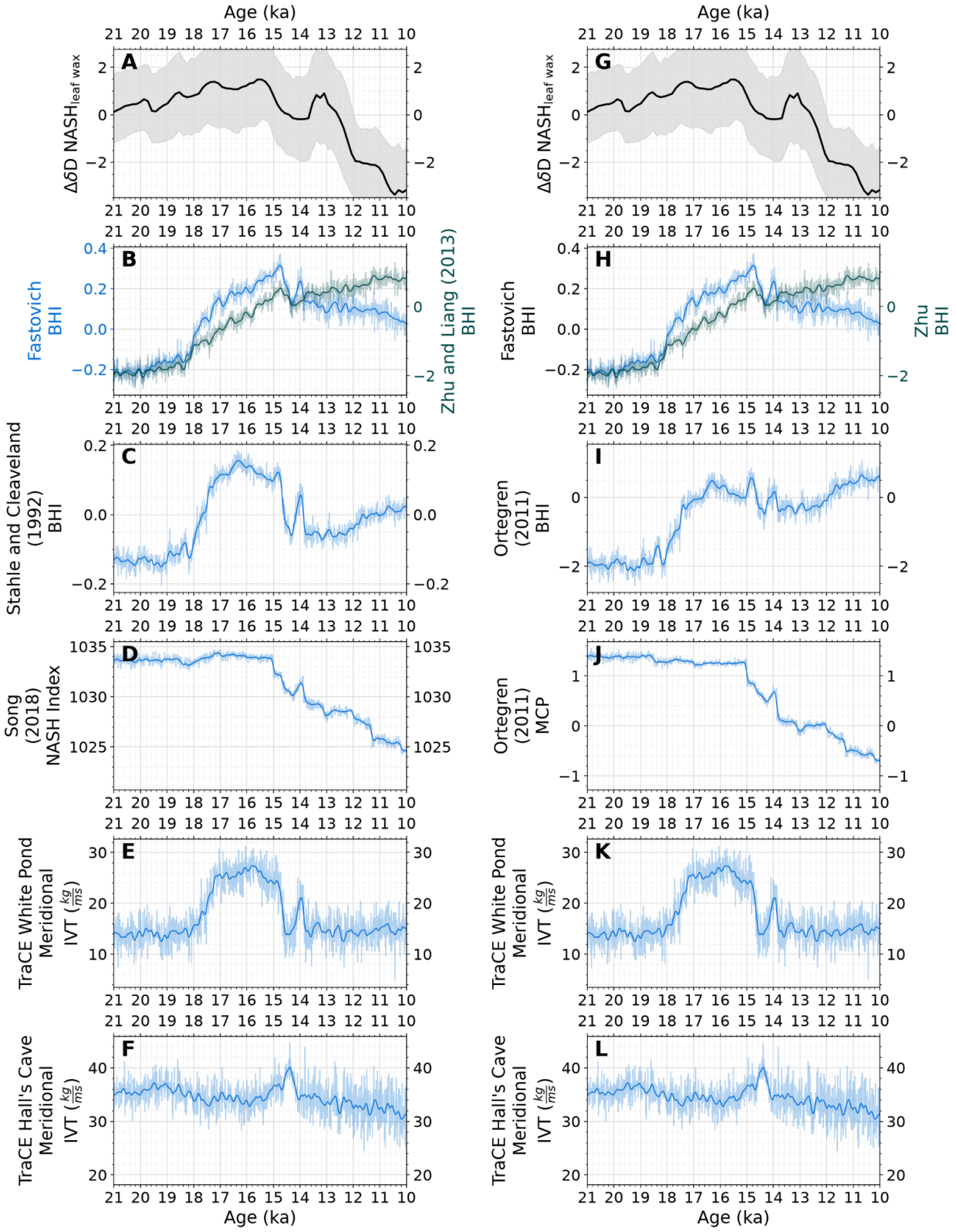


Figure S9. As in Figure S8 but for TraCE-21ka.

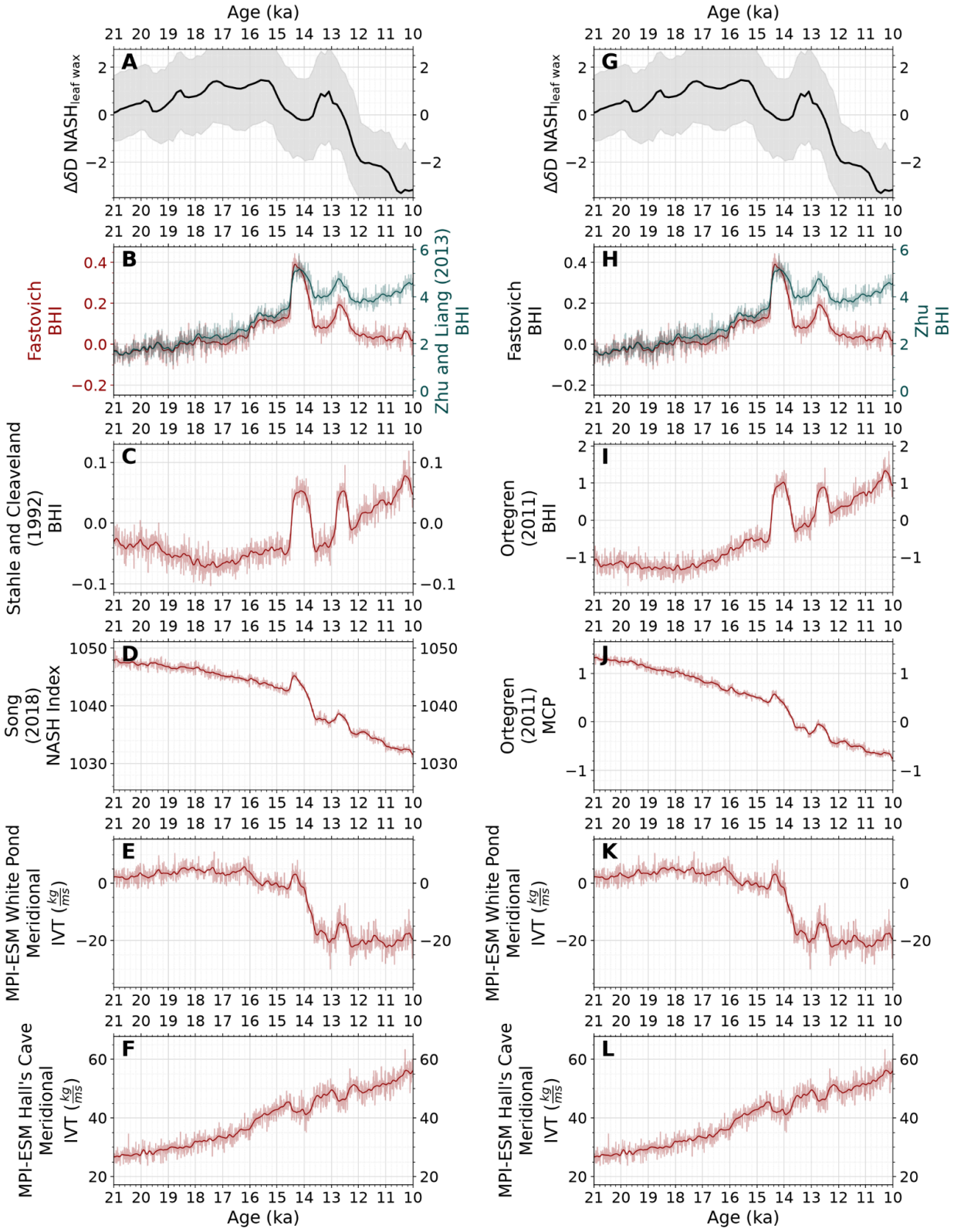


Figure S10. As in Figure S8 but for MPI-ESM1-2-CR.

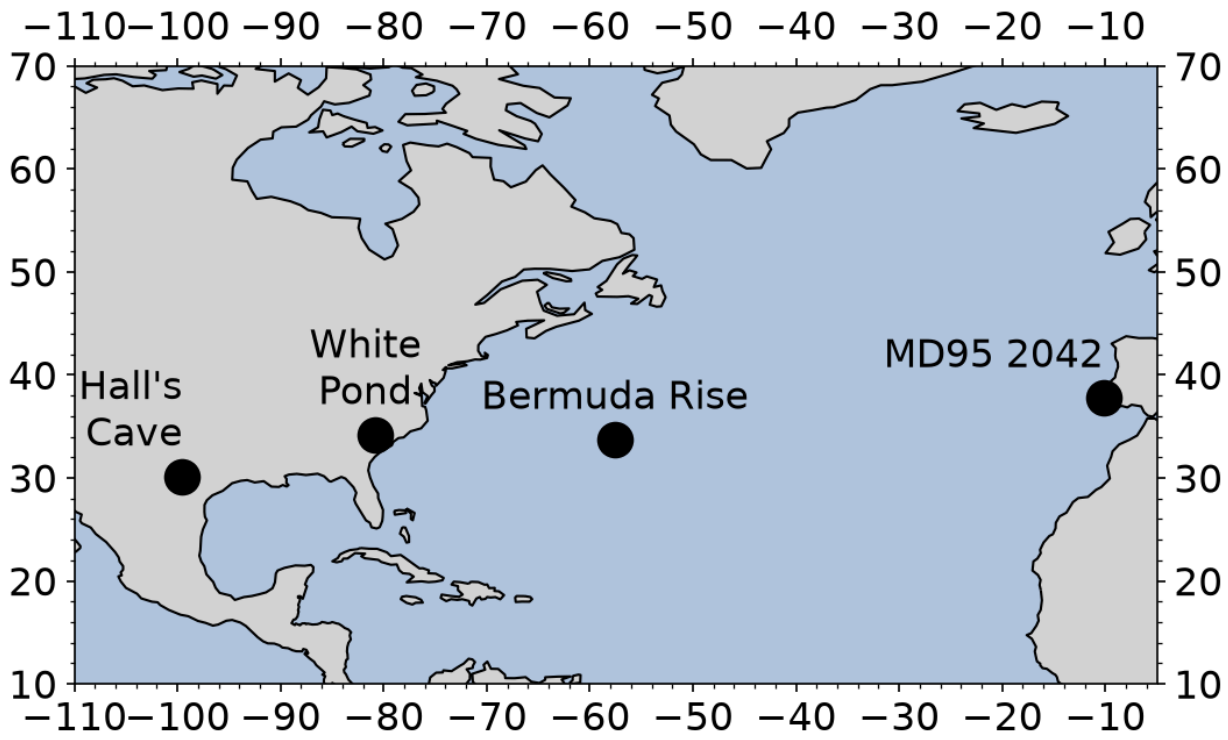


Figure S11. A map of all sites used for analyses in Figures 2 and 4.

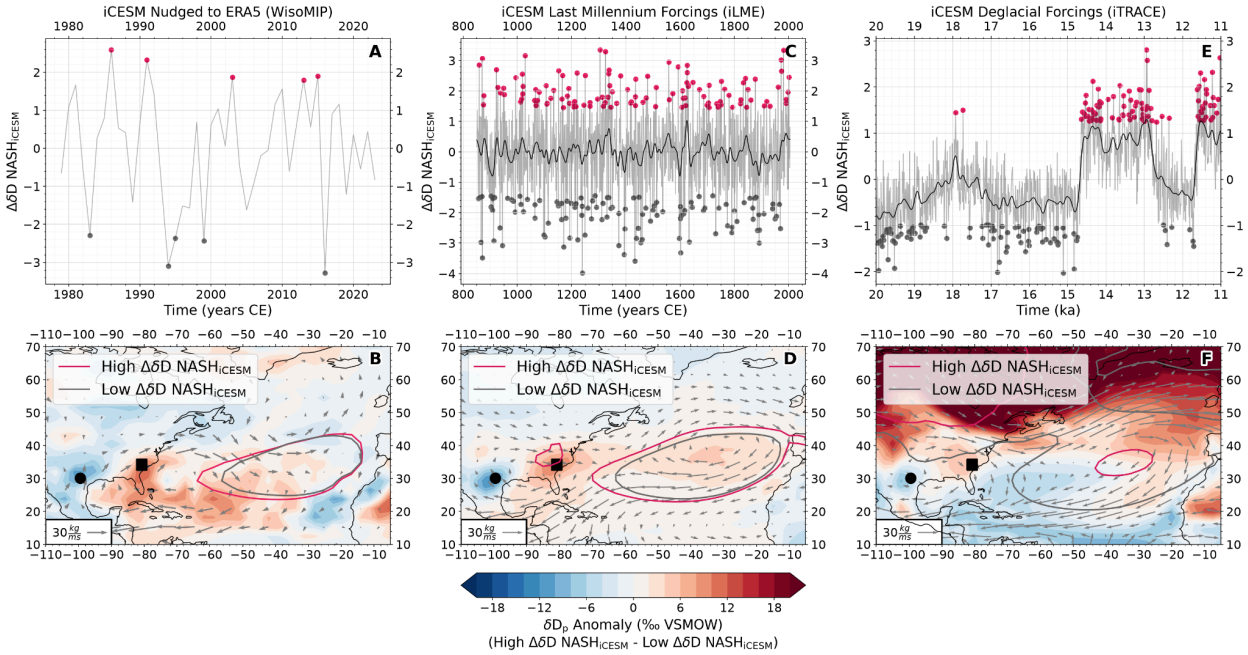


Figure S12. (B, D, F) As in Figure 3, but with the corresponding simulated North Atlantic ΔδD $NASH_{iCESM}$ time series (A, C, E). The pink points correspond to time periods when ΔδD $NASH_{iCESM} \geq$ 90th percentile. The gray points correspond to time periods when ΔδD $NASH_{iCESM} \leq$ 10th percentile.. The anomaly fields in B, D, and F represent the difference in the average of the pink and gray points from A, C, and E and are identical to Figure 3. In panels C and E, the light lines correspond to decadal averages and the dark lines correspond to a Gaussian low-pass filter (σ = 50 years).

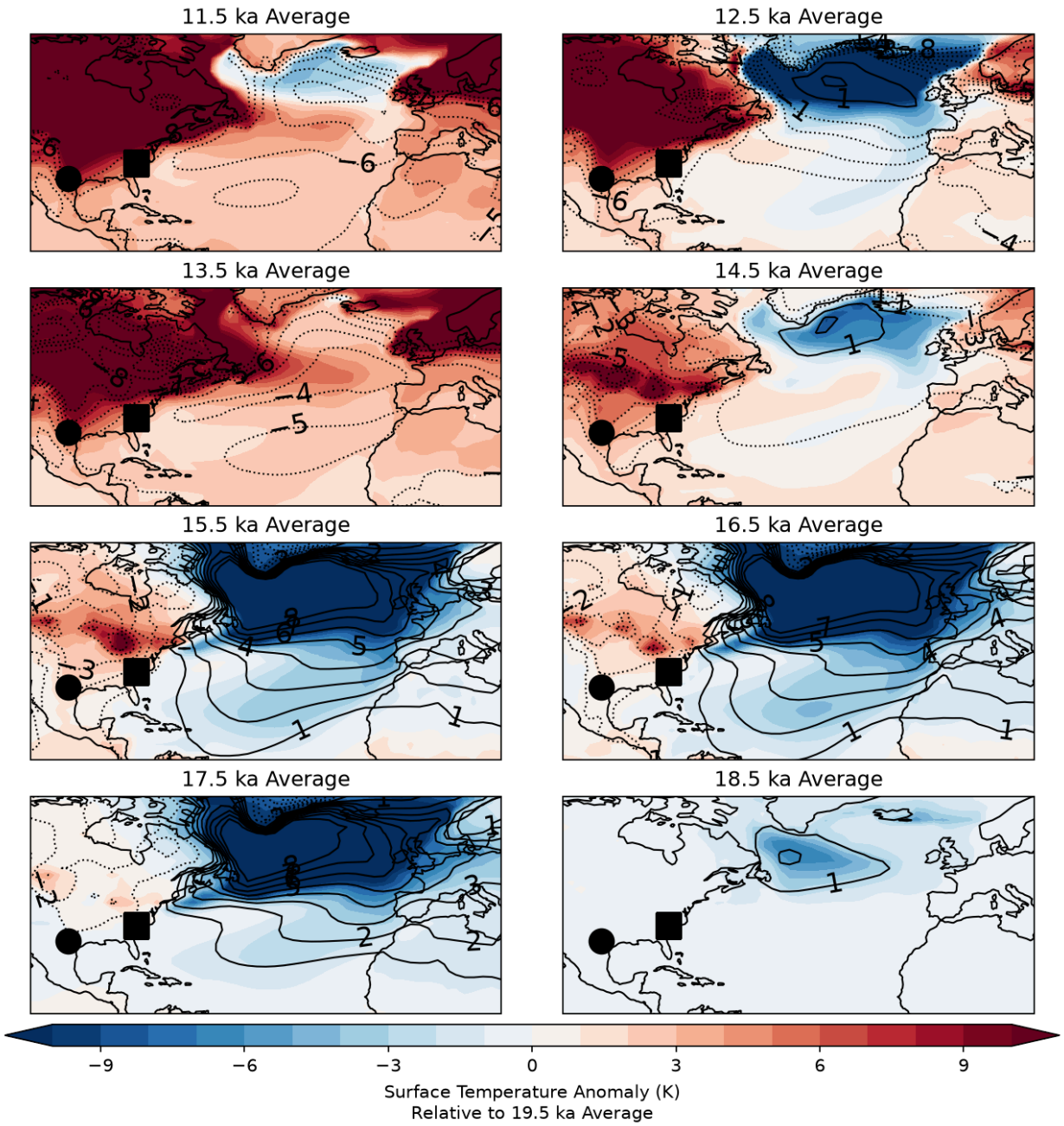


Figure S13. Millennial averages of surface temperature and mean sea level pressure relative to a Last Glacial Maximum baseline (20 to 19 ka). The square and circle points correspond to White Pond and Hall's Cave, respectively.

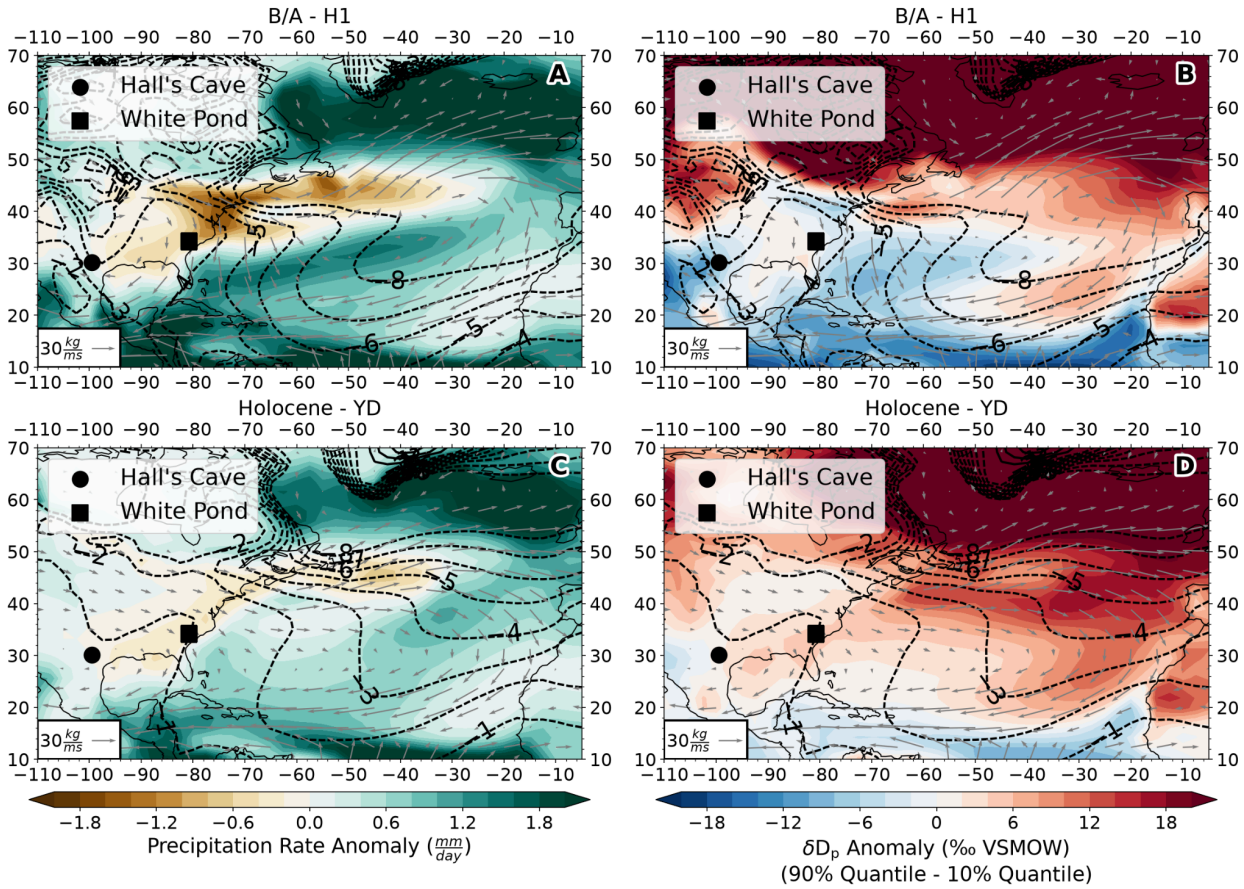


Figure S14. Anomaly fields of simulated (A, C) precipitation rate (filled contours), (B, D) δD_p, (A-D) integrated vapor transport, and (A-D) mean sea level pressure diagnosing the causes of the inverse southeastern North American δD_p gradient-North Atlantic Subtropical High relationship in iTRACE. (A, B) The Heinrich event 1 (temporal average from 17 ka to 15 ka) is subtracted from the Bølling-Allerød (temporal average from 14 ka to 13 ka). Large positive precipitation anomalies in the subtropical and tropical Atlantic from a northward shift in the Intertropical Convergence Zone correspond with decreases in δD_p from the 'amount effect'. Low subtropical and tropical Atlantic δD_p is transmitted to Hall's Cave through easterly anomalies in integrated vapor transport despite decreases in mean sea level pressure. (C, D) The Younger Dryas (temporal average from 12.9 ka to 11.7 ka) is subtracted from the Holocene (temporal average from 11.7 ka to 11 ka, when the iTRACE experiment ends). The spatial patterns in (C, D) mirror (A, B).

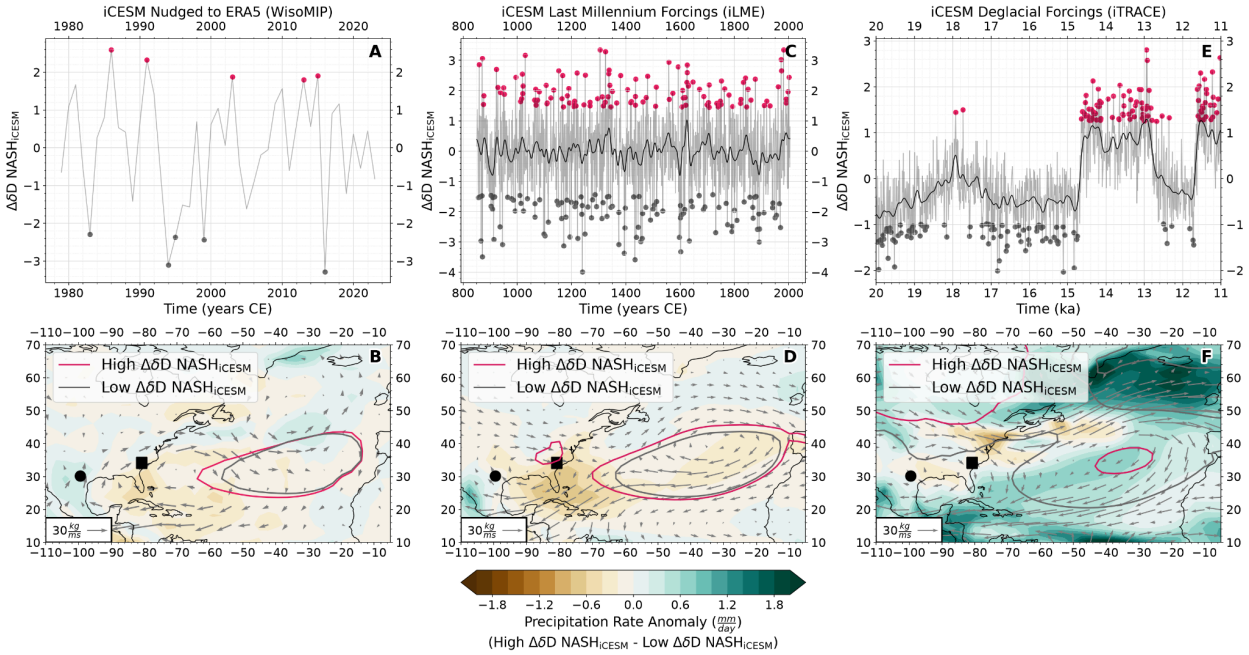


Figure S15. (B, D, F) As in Figure S12 but for simulated precipitation rate anomalies.

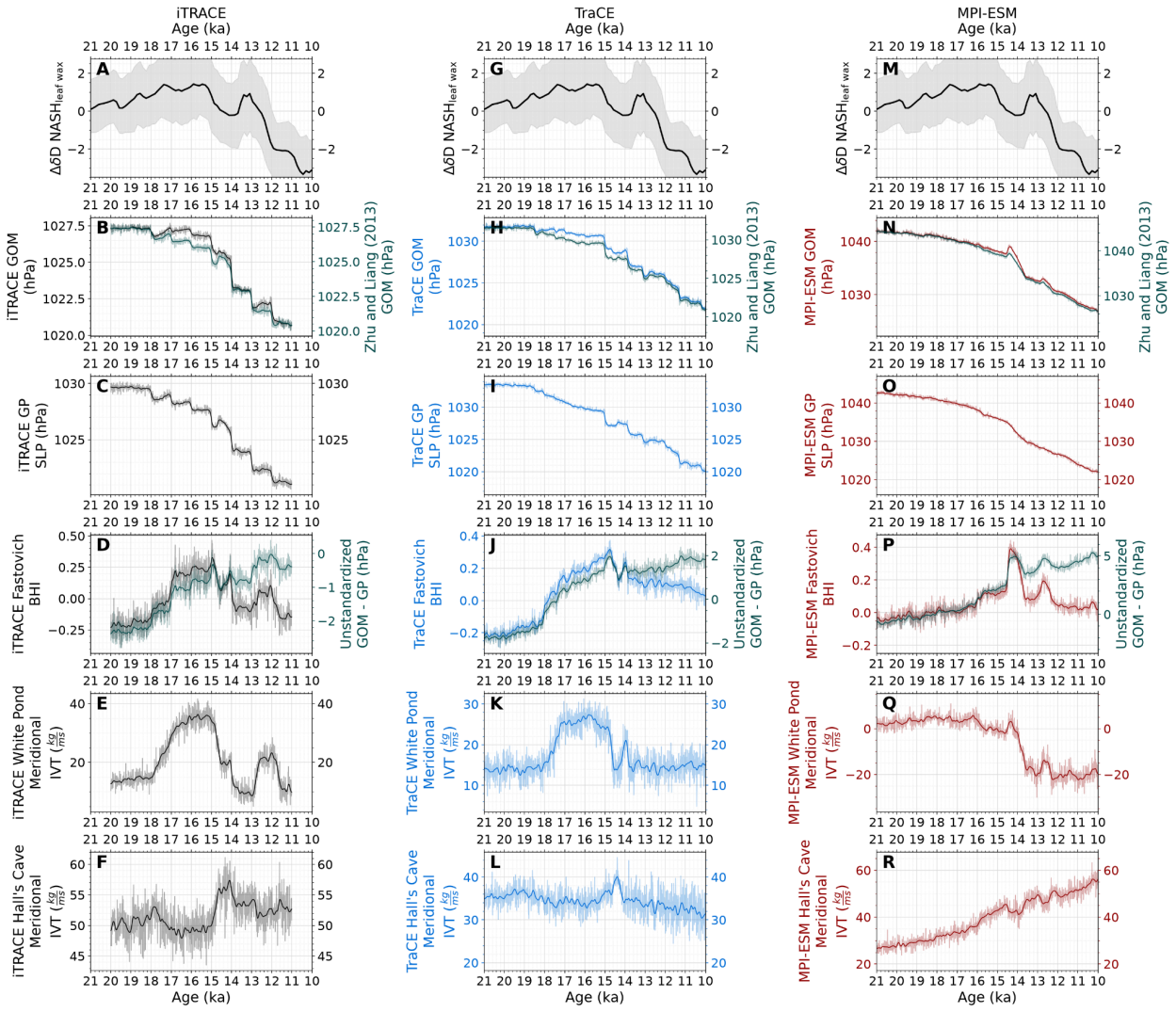


Figure S16. A decomposition of our modifications to the Zhu and Liang (2013) index compared to integrated vapor transport at (E, K, Q) White Pond and (F, L, R) Hall's Cave, and (A, G, M) $\Delta\delta D\ NASH_{leaf\ wax}$ for (A-F) iTRACE, (G-L) TraCE-21ka, and (M-R) MPI-ESM1-2-CR. (B, H, N) The influence of shifting the Gulf of Mexico region ten degrees to the east where the green line corresponds to mean sea level pressure in the original Zhu and Liang (2013) Gulf of Mexico region and the black line correspond to mean sea level pressure shifted ten degrees to the east for (B, black line) iTRACE, (H, blue line) TraCE-21ka, and (N, red line) MPI-ESM1-2-CR. (C, I, O) Mean sea level pressure in the Great Plains region which we do not modify and retain the original region defined in Zhu and Liang (2013). (D, J, P) The influence of standardization on our index where the green line corresponds to our Bermuda High Index with the Gulf of Mexico shifted ten degrees to the east but not standardized before differencing for (D) iTRACE, (J) TraCE-21ka, and (P) MPI-ESM1-2-CR. For comparison, we also present our index but standardized before differencing (as we present in the main text) for (D, black line) iTRACE, (J, blue line), TraCE-21ka, and (P, red line) MPI-ESM1-2-CR. In all panels except A, G, and M, the

light lines correspond to decadal averages and the dark lines correspond to a Gaussian low-pass filter (σ = 50 years).

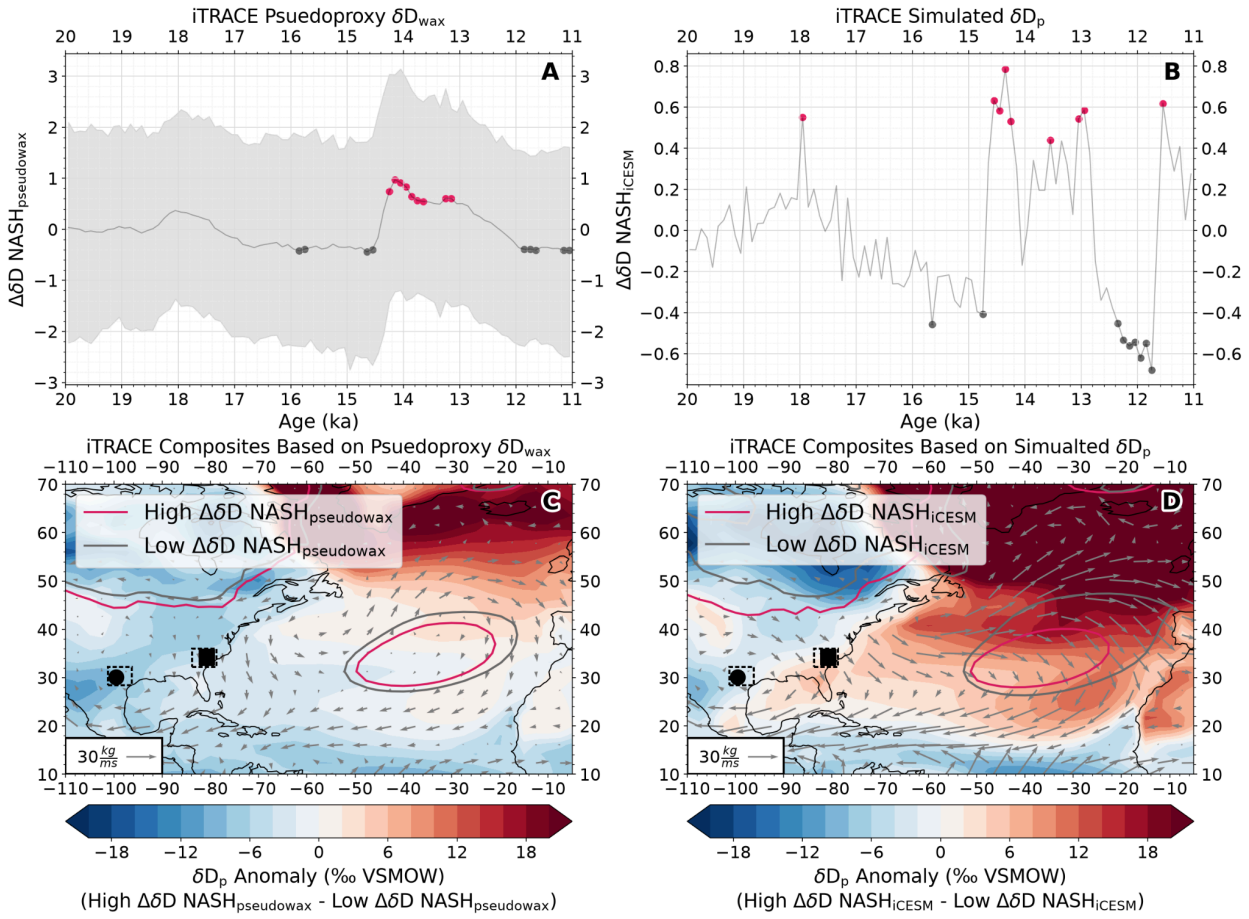


Figure S17. (A) ΔδD $NASH_{pseudoproxy}$ and (B) ΔδD $NASH_{iCESM}$ where pink points correspond to time periods when ΔδD $NASH_{pseudoproxy}$ and ΔδD $NASH_{iCESM} \geq$ 90th percentile. The gray points correspond to time periods when ΔδD $NASH_{pseudoproxy}$ and ΔδD $NASH_{iCESM} \leq$ 10th percentile. The anomaly fields in C and D represent the difference in the average of the pink and gray points from A, C, and E. (C, D) The integrated vapor transport vectors and δD_p filled contours show the anomaly between high-ΔδD $NASH_{pseudoproxy}$/ΔδD $NASH_{iCESM}$ and low-ΔδD $NASH_{pseudoproxy}$/ΔδD $NASH_{iCESM}$. In contrast, the pink contour shows mean sea level pressure during high-ΔδD $NASH_{pseudoproxy}$/ΔδD $NASH_{iCESM}$ years, while the gray contour shows mean sea level pressure during low-ΔδD $NASH_{pseudoproxy}$/ΔδD $NASH_{iCESM}$ years, so the two contours together reveal how the simulated North Atlantic Subtropical High shifts in spatial extent and intensity. These analyses replicate the results presented in Figure 3, but for centennial averages of iTRACE and pseudoproxy leaf-wax biomarkers simulated using PRYSM (Dee et al., 2015) based on input δD_p from iTRACE. We choose to present centennial averages of iTRACE to compare against the time-averaged ΔδD $NASH_{pseudoproxy}$.

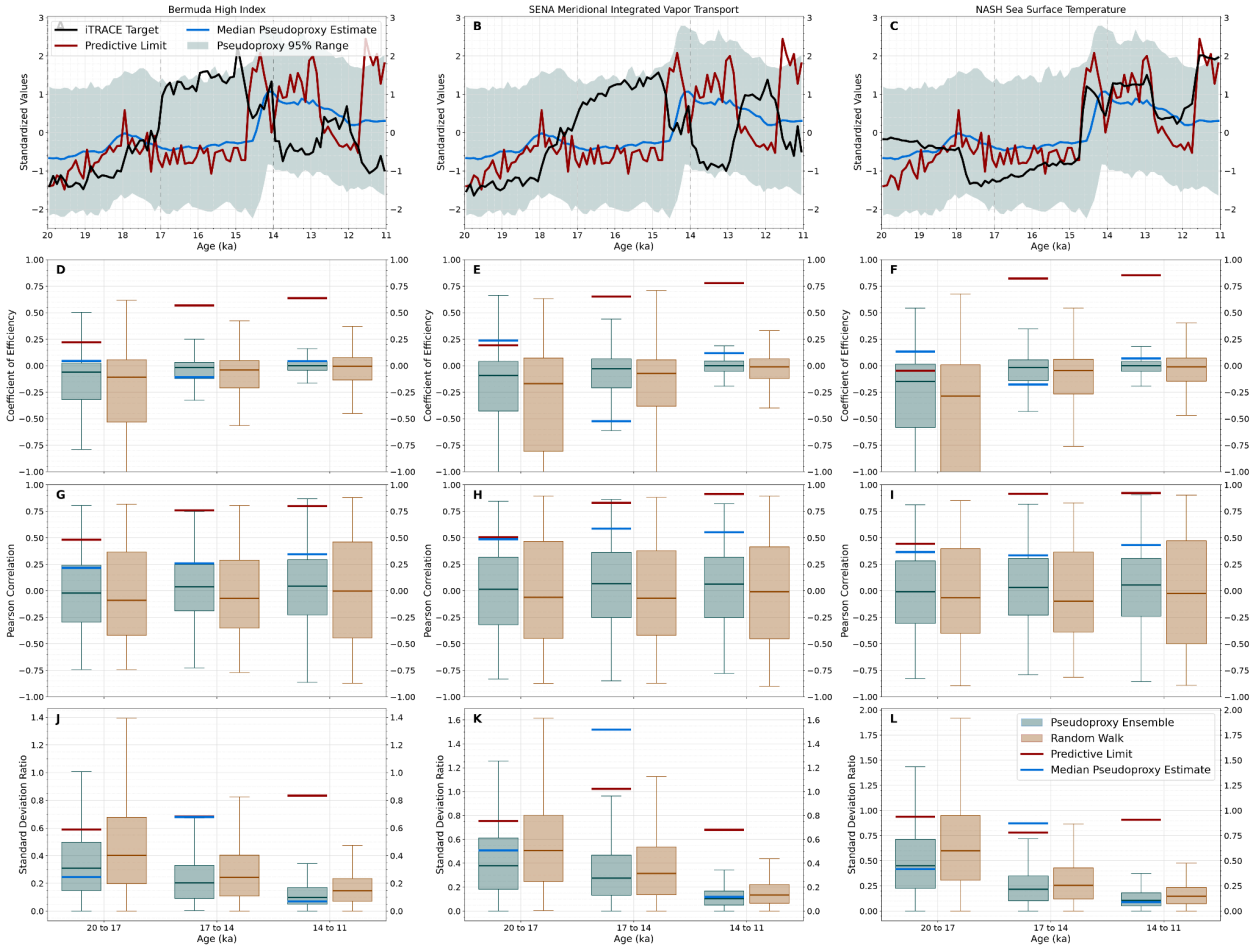


Figure S18. The ability of $\Delta\delta D\ NASH_{pseudoproxy}$ to predict variability in the (A, D, G, J) Bermuda High Index, (B, E, H, K) southeastern North American meridional integrated vapor transport, and (C, F, I, L) sea surface temperatures underneath the North Atlantic Subtropical High measured using the coefficient of efficiency (CE) through leave-one-block-out cross-validation for three blocks. The time series in (A, B, C) correspond to the predictors and target. The predictor is the original target (black line) from iTRACE averaged every 100 years to match the time averaging inherent in the pseudoproxy results. The red line corresponds to $\Delta\delta D\ NASH_{iCESM}$ which is the predictive limit as $\Delta\delta D\ NASH_{pseudoproxy}$ cannot be more predictive than the unmodified iTRACE δD_p that is used as the input for the PRYSM pseudoproxy model. The blue line corresponds to the median $\Delta\delta D\ NASH_{pseudoproxy}$ of the entire ensemble and the green filled area corresponds to the 95% confidence interval of the $\Delta\delta D\ NASH_{pseudoproxy}$ ensemble. The vertical dashed gray lines at 17 ka and 14 ka define the limits for the three blocks used for cross-validation. That is, a linear model was fit for two blocks and used to predict values in the third block (i.e. 20 to 17 ka and 14 to 11 ka and then used to predict values in the 17 to 14 ka block). (D-F) Box plots of the coefficient of efficiency for individual $\Delta\delta D\ NASH_{pseudoproxy}$ ensemble members (green) compared to a random walk null (brown), $\Delta\delta D\ NASH_{iCESM}$ (i.e. the predictive limit, red line), and the median of the $\Delta\delta D\ NASH_{pseudoproxy}$ ensemble (blue line). (G-I) Box plots of the correlation coefficient between predicted and true values from the

leave-one-block-out cross-validation approach for individual ΔδD $NASH_{pseudoproxy}$ ensemble members (green) compared to a random walk null (brown), ΔδD $NASH_{iCESM}$ (i.e. the predictive limit, red line), and the median of the ΔδD $NASH_{pseudoproxy}$ ensemble (blue line). (J-L) Box plots of the standard deviation ratio between predicted and true values from the leave-one-block-out cross-validation approach for individual ΔδD $NASH_{pseudoproxy}$ ensemble members (green) compared to a random walk null (brown), ΔδD $NASH_{iCESM}$ (i.e. the predictive limit, red line), and the median of the ΔδD $NASH_{pseudoproxy}$ ensemble (blue line).